This article has been accepted for publication in IEEE Transactions on Geoscience and Remote Sensing. This is the author's version which has not been fully edited and content may change prior to final publication. Citation information: DOI 10.1109/TGRS.2023.3296958

A Phase-based InSAR Tropospheric Correction Method for Interseismic Deformation Based on Short-period Interferograms

Shuai Wang, Zhong Lu, Bin Wang, Yufen Niu, Chuang Song, Xing Li, Zhangfeng Ma, and Caijun Xu

***Abstract*—The new generation of SAR satellites is serving our long-standing demand for high-resolution crustal deformation over various scales. However, the reliability of InSAR measurements is still limited by varying tropospheric conditions between acquisitions, especially when mapping slow-deforming interseismic deformation. We propose here a new phase-based approach for mapping interseismic deformation using short-period interferograms. Our method formulates the InSAR phase after topographic correction as the sum of three components: (1) spatiotemporally varied turbulent tropospheric phase, (2) topography-correlated stratified tropospheric phase, and (3) interseismic-related deformation assumed to be accumulated at a constant rate. We simultaneously solve for the parameters in the model to avoid overestimating the tropospheric phases, especially when interseismic deformation and tropospheric delays are both coupled with elevation in space. Synthetic tests and practical applications to easternmost Altyn Tagh fault demonstrate that the new method can effectively recover the small-amplitude interseismic deformation caused by fault motion even when the interferograms are dominated by strong tropospheric delays.**

***Index Terms*—InSAR, Tropospheric Correction, Interseismic Deformation.**

I. INTRODUCTION

Over the past few decades, the advent of new generation of radar satellites, such as Sentinel-1, has opened the prospect of mapping Earth's surface deformation through freely open data. This has propelled InSAR from being a specialized research tool to a widely-used powerful monitoring technique for detecting and quantifying surface deformation across a range of scales, from tens of kilometers to global coverage [1], [2]. The current availability of satellite images, with dramatically improved quality and quantity, enable the creation of high-quality crustal velocity map with an accuracy of up to a few millimeters per year and a spatial resolution of tens of meters or finer. Such a deformation map is crucial for investigating a wide range of geoscience problems across various spatial and temporal scales [1].

However, one of the significant challenges in retrieving millimetric interseismic deformation from InSAR measurements is the presence of tropospheric phases caused by the spatial and temporal variabilities of pressure, temperature, and relative humidity between SAR acquisitions. Tropospheric phases, from the point of physical origin, can be typically attributed to two parts: stratified and turbulent components [3]. The former is deemed to be spatially correlated with regional elevation and occasionally exhibits systematic seasonal variations over time. In contrast, the latter is expected to be temporally uncorrelated and essentially characterized by short wavelengths in space. Tropospheric artifacts may occasionally introduce errors up to tens of centimeters in a single interferogram [4], [5], [6], which is considerably greater than the typically observed magnitudes of interseismic signals of interest mostly ranging within a few centimeters [7]. This is especially the case when interseismic deformation and topography are both spatially correlated [4], [5], [8]. Therefore, mitigating errors in InSAR observations, especially the tropospheric artifacts, has always been a crucial issue for the community to improve the accuracy and reliability of interseismic strain accumulation measured by InSAR time series.

As of present, numerous attempts have been made to mitigate the effects of tropospheric phases in InSAR measurement. These methods can be categorized into two types, i.e., the auxiliary data-based approach and the interferometric phase-based correction method [7], [9], depending on the type of data used. From the perspective of auxiliary data, a variety of approaches have been developed using independent measurements of water vapor and hydrostatic pressure, such as GNSS, MODIS, MERIS, ECMWF, ERA5, and MERRA2 [8], [10-18]. Among these, GNSS can provide water vapor observations at the highest temporal resolution (e.g., every 1 min or higher), allowing for

This work was supported by the National Natural Science Foundation of China under Grants 42204001 and 42004002, and also by the Natural Science Foundation of Jiangsu Province under Grant BK20200712. *(Corresponding author: Shuai Wang and Bin Wang)*

Shuai Wang and Bin Wang are with School of Geomatics Science and Technology, Nanjing Tech University, Nanjing, China (e-mail: shwang@njtech.edu.cn; binwangsgg@njtech.edu.cn).

Zhong Lu is with Department of Earth Sciences, Southern Methodist University, Dallas, USA (e-mail: zhonglu@sum.edu).

Yufen Niu is with the School of Mining and Geomatics Engineering, Hebei University of Engineering, Handan, China (e-mail: niuyufen@hebeu.edu.cn).

Chuang Song is with the College of Geological Engineering and Geomatics, Chang'an University, Xi'an, China (e-mail: chuang.song@chd.edu.cn).

Xing Li is with Physical Science and Engineering Division, King Abdullah University of Science and Technology, Thuwal, Saudi Arabia (e-mail: xing.li.1@kaust.edu.sa).

Zhangfeng Ma is with Earth Observatory of Singapore, Nanyang Technological University, Singapore (e-mail: zhangfeng.ma@ntu.edu.sg).

Caijun Xu is with School of Geodesy and Geomatics, Wuhan University, Wuhan, China (e-mail: cjxu@sgg.whu.edu.cn)

the representation of rapidly changing tropospheric turbulence under all-weather conditions [11], [12]. However, the high-quality of such a correction requires a dense and well-distributed GNSS network, which is not globally available. Multi-spectral observations from MODIS and MERIS can provide a high spatial resolution (~250-300 m) of water vapor [10], [13], but they are only available under daytime cloud-free conditions and can only constrain the turbulent component. Moreover, the temporal sampling of these observations is out of sync with the time of SAR acquisitions, typically with a 5-hour difference. Weather models (i.e., MERRA2, ERA5, and ECMWF) and their derivatives (i.e., GACOS) are limited by their low spatial (> 16 km) and temporal sampling (1 or 6 hours). Additional artifacts might be induced when interpolating the tropospheric phases at the time of SAR acquisitions, which often lead to large uncertainties in the corrected interferograms [19]. To summarize, the successful use of external data-based correction methods typically depends on (i) the availability of auxiliary data used in the assimilation process, (ii) the spatial and temporal synchronization between auxiliary data and SAR acquisitions, and (iii) the relatively changing state of the troposphere [15], [20], [21].

From the perspective of the interferometric phase itself, there are also a variety of approaches to correct the interferometric phase errors caused by the troposphere, including the statistical-dependent method [22-24], the blind source separation method (e.g., the independent component analysis method, ICA) [5], and the empirical phase-elevation method [7], [25]. The statistical-dependent method (e.g., spatiotemporal filtering/stacking) relies on the assumption that the tropospheric phases are uncorrelated in time [22], [24], [26]. Although the method is straightforward to apply, it may fail when the assumption is violated (e.g., tropospheric phase is correlated with topography) and it may also impair the temporal resolution of InSAR measurements when the stacking method is utilized. The accuracy of the ICA method depends on the number of principal components [5], and it may not effective when the component sources are correlated statistically, for instance, when the tropospheric phase and the tectonic motion are both correlated with the topography in space. The traditional empirical phase-elevation method assumes a single relationship between phase and topography over an interferogram which limits its applicability to spatially varying topography-correlated troposphere [4], [27], especially over a large spatial scale and/or across different climatic zones. Subsequent empirical methods attempt to overcome this limitation by dividing an interferogram into a series of uniform [21] or quadtree sub-patches [25], [28], or assuming a power law relationship [29]. However, these successions cannot avoid the drawbacks of the empirical methods because (i) the long-wavelength tectonic deformation correlated with topography could be mistaken as stratified atmospheric phases and erroneously removed from the interferograms, and (ii) they cannot reasonably account for turbulent components. It is noteworthy that [30] proposed a phase-based approach that combines tropospheric delays and deformation into a joint model to estimate the tropospheric phases across volcanic areas. Since their method employed only consecutive interferograms, it may not suitable for extracting of interseismic deformation, and the effectiveness when including the deformation term is unclear.

The previous findings highlight that tropospheric correction in InSAR measurements of interseismic deformation is still confronted with big challenges and suggest the need for continued research in this field. In this study, taking advantage of the dense temporal sampling of current SAR acquisitions (e.g., Sentinel-1), we propose an improved phase-based InSAR tropospheric correction method using the short time span (e.g., ≤ 60 days) interferograms. The principle of the method is described in Section II, which includes a preprocessing step to fix phase unwrapping errors. We evaluate the performance of the method using synthetic data and practical data in Sections III and IV respectively. We discuss potential factors may affect the efficiency of our method in Section V, as well as its advantages and limitations. Finally, we draw conclusions in Section VI.

II. Methodology

Since unwrapping errors in interferograms may be as dominant as tropospheric delays in interferometric phase and our proposed approach relies on interferometric phase analysis, we need to tackle any unwrapping errors present in the interferograms before estimating the tropospheric phases and conducting time series analysis. Therefore, to ensure the integrity of our tropospheric correction method, we will first briefly introduce a preprocessing procedure for fixing unwrapping errors (Section II-A) and then introduce in detail the methodology for estimating atmospheric delays using interferograms with short temporal baselines (Section II-B). The complete process flow chart of our method is illustrated in Fig. 1.

A. Fixing Phase Unwrapping Errors Based on Phase Closure Information

Phase unwrapping is a critical step to recover unambiguous phase values from the original phase information measured at modulo 2π rad. The unwrapped phase is expected to behave conservatively when calculating loop closure phase that $\Delta\phi_{ij}^{obs} + \Delta\phi_{jm}^{obs} - \Delta\phi_{im}^{obs} = 0$ [31], where $\Delta\phi_{ij}^{obs}$ is the differential phase between epochs i and j. However, unwrapping errors with the absolute phase difference greater than π between two adjacent points can break the consistency of triplets of interferometric phases and result in a non-zero closure phase. Such errors are common in regions with dense vegetation and/or large contrast in topography relief, where active faults are prone to develop. Therefore, it is crucial to address potential unwrapping errors before applying phase-based tropospheric correction methods; otherwise, they will affect the tropospheric estimations and subsequent time series analysis.

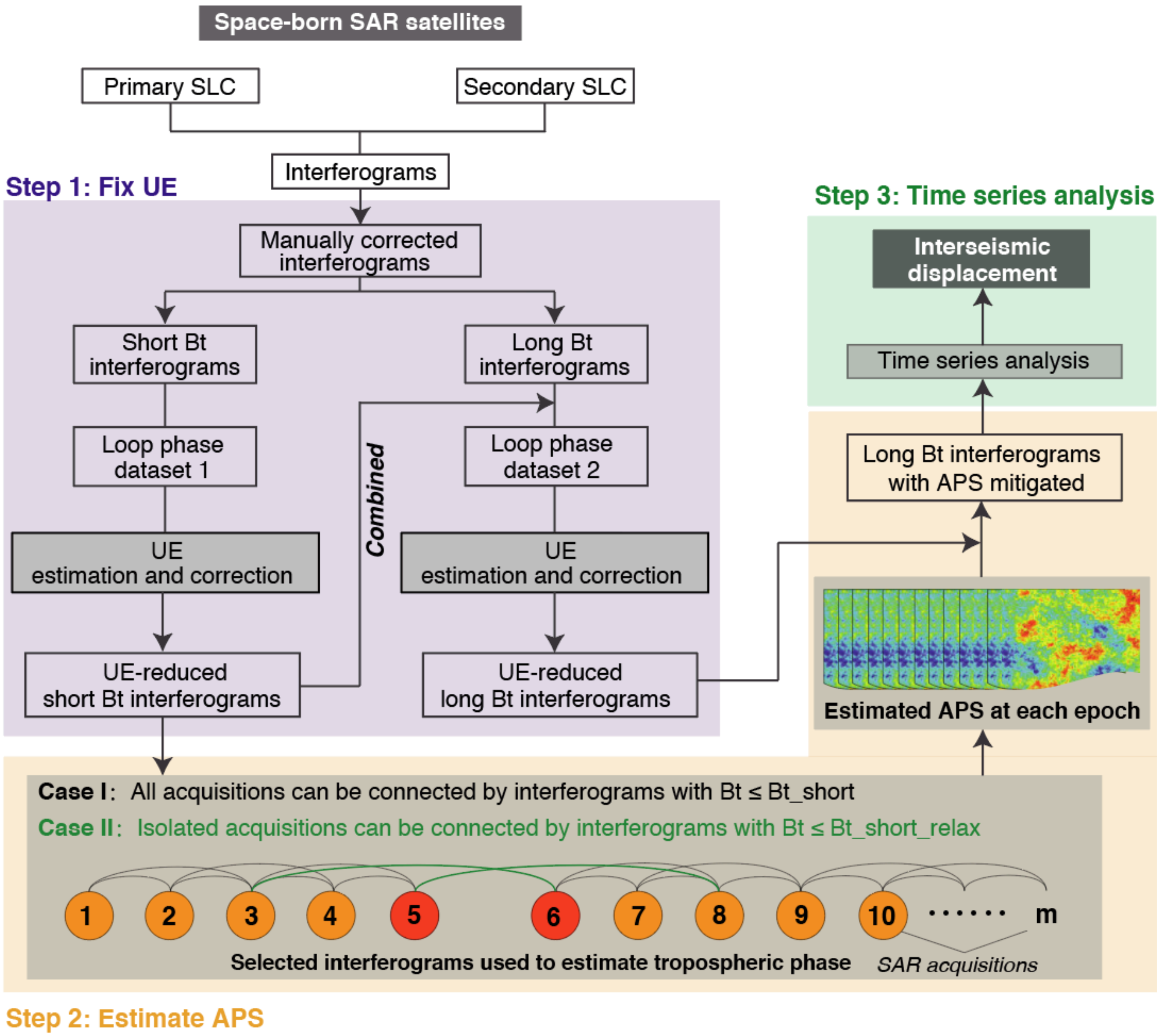

Fig. 1. Flow chart of the proposed interferometric phase-based tropospheric estimation method. UE and APS stand for unwrapping error and atmospheric phase screen, respectively.

One way to identify unwrapping errors is by visually inspecting each interferogram and then manually add an integer-cycle phase offset to the incorrectly unwrapped regions of pixels. However, this can be a time-consuming and labor-intensive process, especially when unwrapping errors occur in multiple interferograms in the same region. In such cases, it may be difficult to correct the errors manually, and the usual practice is by simply detecting/selecting interferograms or relevant pixels with unwrapping errors and discarding them directly [32-34]. This can result in a loss of connectivity in the interferogram network and a decrease in spatiotemporal resolution of the deformation map. To overcome this issue, automatic correction algorithms have been pursued [35], [36]. However, it is important to note that the mathematical equation that links unwrapping errors to the closure phase information in automatic algorithms can be ill-posed and may not always have a unique solution. Automatic approaches are therefore more desirable for highly redundant networks of interferograms with rare unwrapping errors, while not common and highly challenging in interseismic studies.

Unlike previous methods that solve the unwrapping errors using the manual method or automatic approach alone, we propose an approach to solve the problem by combining both. Initially, we manually correct unwrapping errors in interferograms. At this stage, we do not intend to correct all these errors but only focus on specific scenarios where only one interferogram of the triplet has such errors. This correction sets up favorable conditions for the subsequent automatic method, ensuring a unique solution to the maximum extent possible. We follow [35]'s idea of using the least absolute shrinkage and selection operator to do the automatic correction, but we apply a two-step procedure. First, we use loop closure phases (Loop phase dataset 1 in Fig. 1) calculated from short-period (e.g., ≤ 60 days) interferograms to estimate unwrapping errors in these interferograms. Then, we use the long-period (e.g., 400 - 500 days) interferograms together with the unwrapping error-reduced short-period interferograms to calculate another set of closure phase loops (Loop phase dataset 2 in Fig. 1), which can provide strong constraints on unwrapping errors in the long-period interferograms. These interferograms are believed to have more phase contributions from interseismic deformation.

B. Estimation of Atmospheric Delays From Short Temporal Baseline Interferograms

At each pixel, the phase of a topography-removed InSAR interferogram with acquisitions at dates t_1 and t_2 can be expressed as:

$$\Delta\phi_{12}^{\text{obs}} = \Delta\phi_{12}^{\text{defo}} + \Delta\phi_{12}^{\text{dry}} + \Delta\phi_{12}^{\text{wet}} + \phi_{12}^{\text{noise}} \tag{1}$$

where $\Delta\phi_{12}^{\text{defo}}$ is the radar phase change due to surface deformation that occurs during the time period of two acquisitions at dates t_1 and t_2. $\Delta\phi_{12}^{\text{dry}}$ is the hydrostatic tropospheric phase delay spatially correlated with topography, and $\Delta\phi_{12}^{\text{wet}}$ the turbulent tropospheric phase delay related to spatially varying water vapor content in the troposphere. ϕ_{12}^{noise} is the noise term attributed to decorrelation caused by spatial-temporal variabilities in scattering properties.

Even though the elevation-dependent tropospheric delay could vary over large-scale areas, the simple linear function can still to the first order describe the spatial variability of the troposphere over an interferogram. Thus, for simplicity, in this study, we assume a single linear phase-elevation relationship to represent the hydrostatic tropospheric phase delay over an interferogram. The unmodeled heterogenous elevation-dependent delay might be incorporated into the wet delay estimation. Previous studies showed the real turbulent tropospheric phase can also exhibit long wavelength behavior [37]. We include two parts in the parametric model to account for the turbulent phase: one accounts for the short wavelength wet delay and the other that accounts for the long wavelength wet delay. Thus, we further rewrite (1) as follows with the rationale rooted in the distinct spatiotemporal dependencies of these parameters:

$$\phi_{12}^{\text{obs}} = vt_{12} + k_2h - k_1h + a_2 - a_1 + b_2x - b_1x + c_2y - c_1y + \phi_2^{\text{wet}} - \phi_1^{\text{wet}} + \phi_{12}^{\text{noise}} \tag{2}$$

where v is the deformation rate for the current pixel assumed to be constant throughout the observation interval. t_{12} is the time period between acquisitions 1 and 2 with the unit in years. k_i is the coefficient relating topography (h) to the absolute hydrostatic phase delays for the ith SAR acquisition. a_i, b_i and c_i are the coefficients used to calculate the long wavelength wet delay for the ith SAR acquisition; x and y are the coordinates of pixels along the range and azimuth directions respectively. ϕ_i^{wet} represents the short wavelength wet delay at the ith epoch. The effect of decorrelation noises on the short-period (e.g., ≤ 60 days) interferograms (typically with good coherence) is relatively small when compared with long-period interferograms. They, if exist, can be also suppressed through spatial filtering or multi-looking during the formation of interferograms. Therefore, only short-period interferograms, typically assumed to be of high quality, are used in our method to estimate the tropospheric delays.

Assuming we have a stack of N unwrapped interferograms $\boldsymbol{d} = [d_1, d_2, \ldots, d_N]^{\text{T}}$ produced from M scenes acquired at epochs of $(t_1, t_2, \ldots, t_M)$ with P pixels that preserve coherence. For the deformation rate (i.e., v), each pixel has its own corresponding value, and thus there are total P deformation parameters needed to be solved, i.e., $(v_1, v_2, \ldots, v_P)$. For the topography-correlated tropospheric delays, each epoch has one parameter (i.e., k), and thus there are $1 \times M$ coefficients needed to be solved, i.e., $(k_1, k_2, \ldots, k_M)$. For the short wavelength turbulent delays, there are M parameters per pixel $(\phi_1^{\text{wet}}, \phi_2^{\text{wet}}, \ldots, \phi_M^{\text{wet}})$, and totally $P \times M$ parameters needed to be solved, i.e., $(\phi_{1,1}^{\text{wet}}, \phi_{1,2}^{\text{wet}}, \ldots, \phi_{P,M}^{\text{wet}})$. For the long wavelength turbulent delays, each epoch has three parameters (i.e., a, b and c), and thus there are $3 \times M$ aggregate coefficients needed to be solved, i.e., $(a_1, a_2, \ldots, a_M)$, $(b_1, b_2, \ldots, b_M)$ and $(c_1, c_2, \ldots, c_M)$.The observation equation can be formulated as (3):

$$\overbrace{\begin{bmatrix} \boldsymbol{G}_1 & 0 & \cdots & 0 & \boldsymbol{G}_{2,1} & \boldsymbol{G}_{3,1} \\ 0 & \boldsymbol{G}_1 & \cdots & 0 & \boldsymbol{G}_{2,2} & \boldsymbol{G}_{3,2} \\ \vdots & \vdots & \ddots & \vdots & \vdots & \vdots \\ 0 & 0 & \cdots & \boldsymbol{G}_1 & \boldsymbol{G}_{2,M} & \boldsymbol{G}_{3,M} \end{bmatrix}}^{\boldsymbol{G}} \cdot \overbrace{\begin{bmatrix} \boldsymbol{X}_1 \\ \boldsymbol{X}_2 \\ \boldsymbol{X}_3 \end{bmatrix}}^{\boldsymbol{X}} = \overbrace{\begin{bmatrix} \Delta\phi_{12,1}^{\text{obs}} \\ \Delta\phi_{13,1}^{\text{obs}} \\ \Delta\phi_{23,1}^{\text{obs}} \\ \vdots \\ \Delta\phi_{M(M\text{-}1),1}^{\text{obs}} \\ \vdots \\ \Delta\phi_{12,P}^{\text{obs}} \\ \Delta\phi_{13,P}^{\text{obs}} \\ \Delta\phi_{23,P}^{\text{obs}} \\ \vdots \\ \Delta\phi_{M(M\text{-}1),P}^{obs} \end{bmatrix}}^{\boldsymbol{b}_{\text{obs}}} \tag{3}$$

where,

$$\boldsymbol{G}_1 = \begin{bmatrix} -1 & 1 & 0 & \cdots & 0 & t_{12} \\ -1 & 0 & 1 & \cdots & 0 & t_{13} \\ 0 & -1 & 1 & \cdots & 0 & t_{23} \\ \vdots & \vdots & \vdots & \ddots & \vdots & \vdots \\ 0 & 0 & 0 & \cdots & 1 & t_{M,M\text{-}1} \end{bmatrix} \quad \boldsymbol{G}_{3,i} = \begin{bmatrix} -h_i & h_i & 0 & \cdots & 0 \\ -h_i & 0 & h_i & \cdots & 0 \\ 0 & -h_i & h_i & \cdots & 0 \\ 0 & 0 & 0 & \cdots & h_i \end{bmatrix}$$

$$\boldsymbol{G}_{2,i} = \begin{bmatrix} -1 & 1 & 0 & \cdots & 0 & -x_i & x_i & 0 & \cdots & 0 & -y_i & y_i & 0 & \cdots & 0 \\ -1 & 0 & 1 & \cdots & 0 & -x_i & 0 & x_i & \cdots & 0 & -y_i & 0 & y_i & \cdots & 0 \\ 0 & -1 & 1 & \cdots & 0 & 0 & -x_i & x_i & \ldots & 0 & 0 & -y_i & y_i & \cdots & 0 \\ \vdots & \vdots & \vdots & \ddots & \vdots & \vdots & \vdots & \vdots & \ddots & \vdots & \vdots & \vdots & \vdots & \ddots & \vdots \\ 0 & 0 & 0 & \cdots & 1 & 0 & 0 & 0 & \ldots & x_i & 0 & 0 & 0 & \cdots & y_i \end{bmatrix}$$

$$\boldsymbol{X}_1 = \begin{bmatrix} \phi_{1,1}^{\text{wet}} & \phi_{2,1}^{\text{wet}} & \phi_{3,1}^{\text{wet}} & \cdots & \phi_{M,1}^{\text{wet}} & v_1 & \cdots & \phi_{1,P}^{\text{wet}} & \phi_{2,P}^{\text{wet}} & \phi_{3,P}^{\text{wet}} & \cdots & \phi_{M,P}^{\text{wet}} & v_P \end{bmatrix}^{\text{T}} \tag{4}$$

$$\boldsymbol{X}_2 = \begin{bmatrix} a_1 & a_2 & a_3 & \cdots & a_M & b_1 & b_2 & b_3 & \cdots & b_M & c_1 & c_2 & c_3 & \cdots & c_M \end{bmatrix}^{\text{T}}$$

$$\boldsymbol{X}_3 = \begin{bmatrix} k_1 & k_2 & k_3 & \cdots & k_M \end{bmatrix}^{\text{T}}$$

To obtain an optimal estimate of parameters, one can solve (3) directly. However, the number of parameters in (3) may reach millions or even more, depending on the scope of the study area and the size of grid cells provided. It may be impractical or even unnecessary to solve for all these parameters in a single solution, as in [30]. Instead, we employ a two-step procedure to estimate these parameters and enhance computational efficiency. As indicated by (2), the relevant parameters associated with hydrostatic topography-correlated delay and long wavelength wet delay maintain the same values for each pixel within a given epoch. Consequently, in the first step, we use only InSAR observations at decimated pixels (e.g., decimated by a factor of 10 × 10 in range and azimuth directions) to estimate all parameters in (3) using the minimum norm approach as $\boldsymbol{X} = \boldsymbol{G}^{\mathrm{T}}(\boldsymbol{G}\boldsymbol{G}^{\mathrm{T}})^{-1}\boldsymbol{b}$. We can compute the topography-correlated and long wavelength delays for all pixels in this step, but the estimations of the short wavelength delay and deformation rate are limited to the decimated pixels. In the second step, we subtract the topography-correlated and long wavelength delays estimated in the first step, and use the residual phases at all coherent pixels to estimate the deformation rate and short wavelength turbulent delay for each epoch. Finally, we obtain the total atmospheric phase screen for each epoch by summing the turbulent phase component and the stratified phase component. The estimated total phase delays on each epoch, synchronized in space and time with SAR acquisitions, are removed from the long-period interferograms utilized for time series analysis (Step 3 in Fig. 1).

Occasional inconsistencies have been observed in the spatial coverage of the Sentinel-1 Terrain Observations with Progressive Scans (TOPS) SAR data [32], [38], particularly in the early stages of the mission. Consequently, some frames may have extended acquisition gaps in time (several months or more), leading to some SAR epochs (such as acquisitions 5 and 6 in Fig. 1) not being connected by interferograms with a temporal baseline of smaller than the defined threshold (denoted as Bt_short) (e.g., Bt_short = 36 days). For this case, we prefer to use a relaxed temporal baseline threshold (denoted as Bt_short_relax) (e.g., Bt_short_relax = 60 days) and select relevant interferograms to avoid any unconnected acquisitions. It should be noted that we only select the one with the relatively shortest temporal baseline among the interferograms with temporal baseline ≤ Bt_short_relax. In an ideal scenario, we incorporate all interferograms with temporal baselines of ≤ Bt_short to solve for the parameters in (3) if SAR epochs have good connectivity (i.e., as case I shown in Fig. 1), so as to minimize any decorrelation noise.

III. Validation With Synthetic Data

A. Synthetic Data

To test the ability of our method in separating tectonic deformation from tropospheric noises, we conduct a series of analyses on synthetic data containing realistic tropospheric noise and a simulated deformation signal caused by fault-slip motion. We use the Toolbox for Reducing Atmospheric InSAR Noise (TRAIN) [7], [29] to simulate the tropospheric phases for 112 epochs of Sentinel-1 SAR images from ascending track 172 over the northeast Altyn Tagh fault in the north Tibetan Plateau, spanning from 04 April 2017 to 26 March 2021, based on global weather data ERA5. From these epochs, we generate a total of ~1,050 interferograms, including ~630 ones with short temporal baselines (12 - 96 days; Fig. S1) and ~420 ones with long temporal baselines (400 - 500 days; Fig. S2). We use the classical two-dimensional elastic interseismic deformation model [39] to simulate the surface motions of the Altyn Tagh fault assuming a left-lateral strike-slip of 10 mm/yr from 10 km downward. The simulated deformation rates are projected onto the radar line-of-sight (LOS) direction based on the local incidence and azimuth angles of the SAR image. We calculate the phase component due to fault-slip motion for each interferogram by multiplying the simulated mean LOS velocity by their respective time periods (e.g., Fig. 2a2). We then sum these results with the corresponding atmospheric phases simulated above to obtain the final synthetic interferograms (e.g., Fig. 2a1). We observe that the simulated tropospheric phases are large enough in magnitude to overwhelm the real deformation signal to a certain extent, which describes a more realistic scenario in InSAR studies of interseismic strain, and thus more conducive for us to evaluate the performance of our method. It is important to note that the synthetic interferograms did not contain any phase unwrapping errors, and the preprocessing procedure to fix unwrapping errors will be used in the real data in Section IV.

To quantify the effectiveness of our method, in the following two subsections, we conduct a comparison between the tropospheric-corrected interferograms and the simulated true fault motion signals that were initially utilized to generate the synthetic interferograms. Additionally, we also compare our results with the outcomes from two other frequently employed phase-based correction methods: the empirical linear phase-elevation correction [4] and the common-scene-stacking (CSS) method [40], [41].

B. Reduction in Phase Variability

Fig. 2a1 presents an example synthetic interferogram with an initial standard deviation (STD) of ~7.61 rad. It is evident that the atmospheric signal, calculated from ERA5, consists of a positive LOS change with long wavelengths over high-elevation regions and a negative LOS change with relatively long wavelengths over low-elevation regions. After making corrections using the three methods, the atmospheric noises have been reduced to varying degrees, with the STD of the interferogram decreasing to 3.63, 2.17, and 0.68 rad for the simple empirical method, the CSS, and our algorithm respectively. However, we observe that the empirical linear approach fails to describe the regional spatial variabilities of the atmospheric signals. This results in the corrected outcome significantly deviating from the true deformation in spatial pattern (Figs. 2b1 and 2b2). Although the CSS method appears to perform better than the empirical approach, it could only eliminate a portion of the tropospheric delays in the interferogram (Figs. 2c1 and 2c2). The existence of temporal correlated stratified tropospheric delays could violate the assumption of the CSS method, introducing residual tropospheric noise to the rate map and thus degrading its performance. As expected, our method outperforms the other two methods by reducing the local phase variations with the lowest STD of 0.68 rad, owing to its ability to consider the spatial and temporal variabilities of the troposphere.

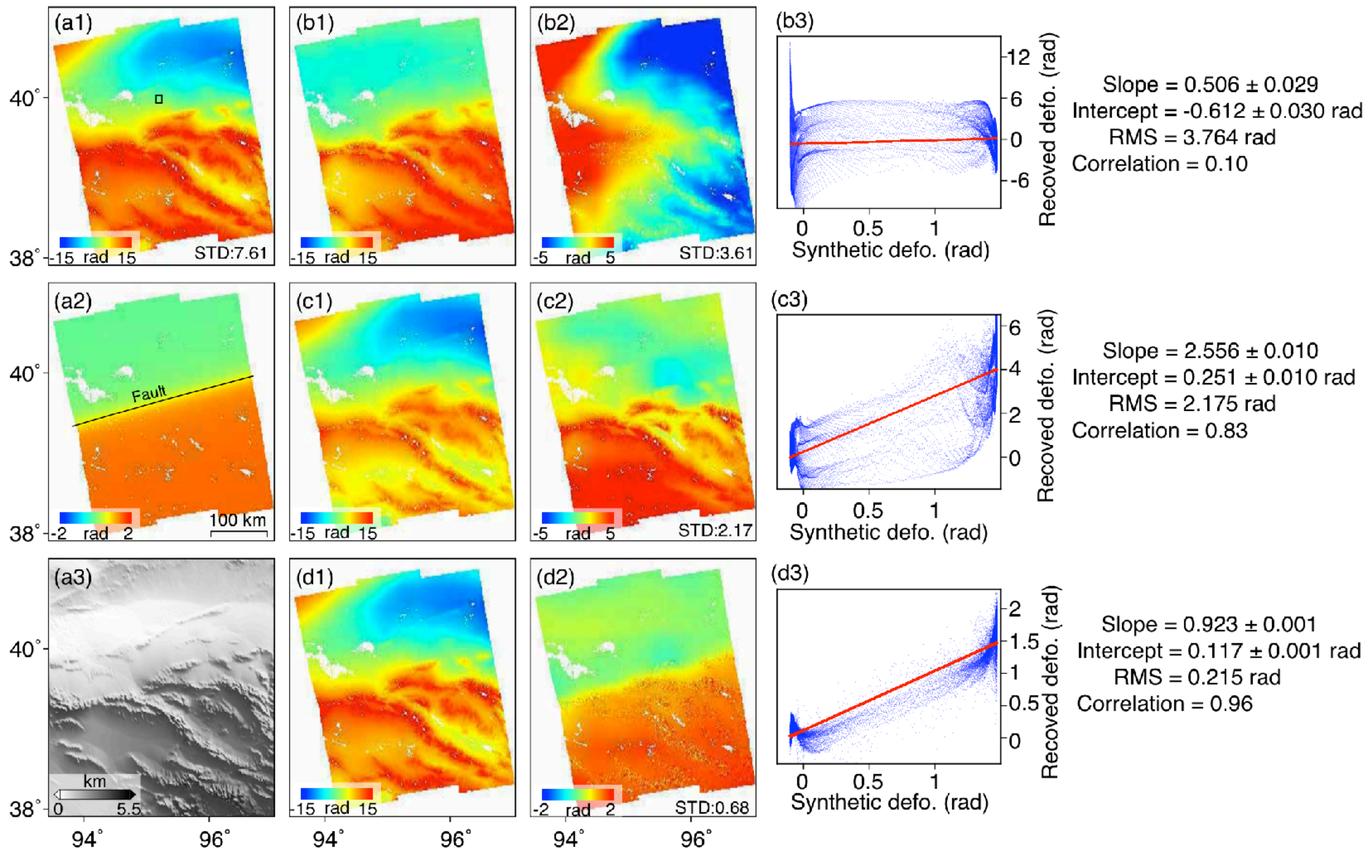

Fig. 2. Tropospheric correction assessment with an example simulated interferogram (20170826-20181101). (a1) Simulated interferogram by combining the ERA5-derived tropospheric phase and the simulated deformation signals due to fault motion (a2). (a3) Regional elevation across the northeast Altyn Tagh fault. (b1) Tropospheric phase estimated from the empirical method. (b2) Corrected interferogram obtained by removing (b1) from (a1). (b3) Scatter plots of the simulated and recovered tectonic deformation. Note that phases in all panels are referenced to the reference window outlined in (a1).(c1-c3) Same as (b1-b3) but for the CSS method. (d1-d3) Same as (b1-b3) but for our proposed method.

We further conduct a comprehensive analysis of the tropospheric correction by calculating of the fitting slope, correlation and root-mean-square (RMS) of the difference between the recovered and simulated tectonic deformation (as shown in Figs. 2b3, 2c3 and 2d3). We can see that our method achieves a slope of ~1, an intercept of ~0, a correlation of 0.96, and an RMS of only 0.215 rad. In contrast, the respective indicators for the empirical linear method are 0.506, -0.612, 0.10, and 3.764 rad; those for the CSS method are 2.556, 0.251, 0.83, and 2.175 rad. An RMS value close to 0 and slope and correlation close to 1 indicate a small deviation between the recovered and the true deformation, thus implying a satisfactory correction of the atmospheric phase. The proposed method outperforms the phase elevation model and CSS method for the example interferogram.

In addition to the example interferogram, we also examine the statistic results (in Fig. 3) for all long temporal baseline interferograms involved in the displacement time series analysis. From the empirical linear and the CSS methods, a certain portion of the interferograms still exhibit significant phase variability with a negative reduction in STD (Fig. 3a), meaning that additional noise was introduced during the corrections. Specifically, for the empirical linear method, only 63% of the interferograms achieve a positive STD reduction (with just 26% experiencing a reduction greater than 0.5), so, this means that 37% of the interferograms were contaminated by additional noise (Fig. 3b). The CSS correction is more effective than the linear method, with 82% of the interferograms experiencing a positive STD reduction (with 49% exhibiting a reduction greater than 0.5) (Fig. 3b). Visual inspection of individual interferograms suggests that the CSS method appears to be more accurate in predicting the spatiotemporal variability of tropospheric properties than the empirical method, although the magnitude may sometimes be incorrect. Overall, the proposed method achieves the best corrections, with ~95% of interferograms experiencing an STD reduction greater than 0.5 (Fig. 3b).

This article has been accepted for publication in IEEE Transactions on Geoscience and Remote Sensing. This is the author's version which has not been fully edited and content may change prior to final publication. Citation information: DOI 10.1109/TGRS.2023.3296958

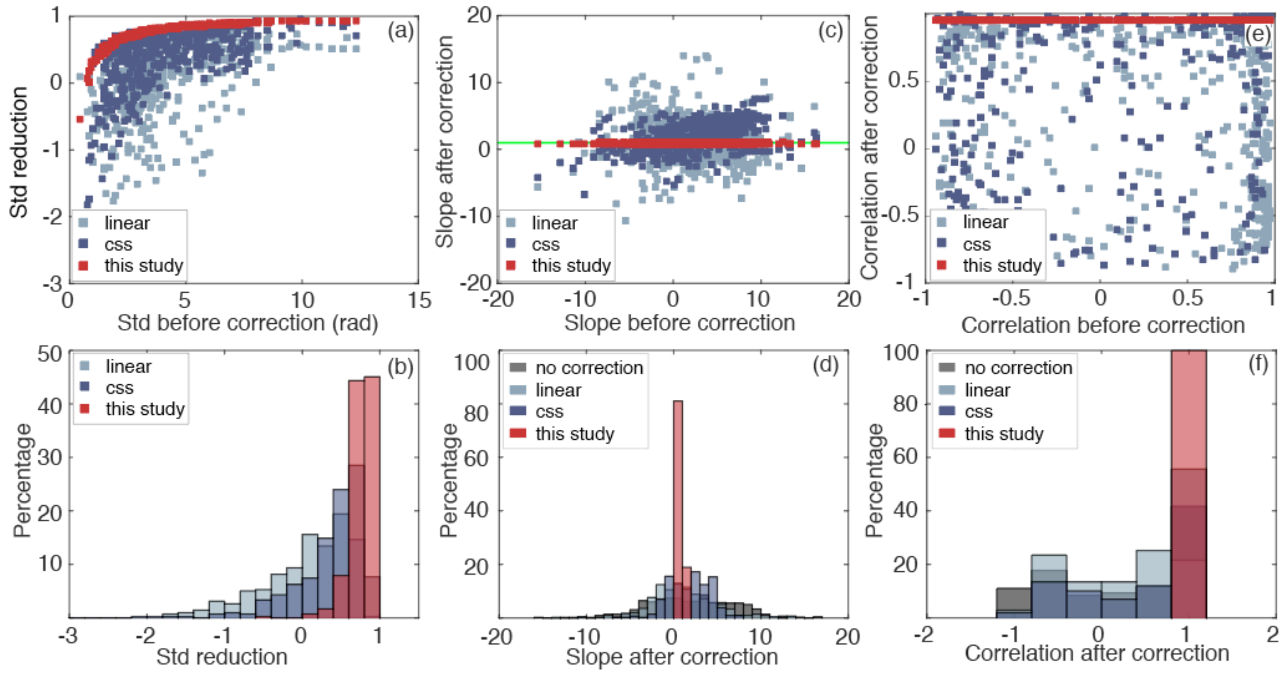

Fig. 3. Quality assessments of the atmospheric corrections on the simulated long-period (400 - 500 days) interferograms. (a) Scatter plots of the STD reductions of the interferograms after the corrections of the empirical method, the CSS, and the proposed method. (b) Histograms of the STD reductions for panel (a). (c) and (d) Same as (a) and (b) but for the slopes between the recovered tectonic deformation and the corresponding true values. (e) and (f) are same as (c) and (d) but for the correlations.

From the aspect of slopes between the corrected and simulated deformation interferograms, we can see that the improvement is minor for both the linear method and the CSS approach, which still varies over a wide range (from -15 to 16) after the corrections (Figs. 3c and 3d). Negative slopes suggest an overestimation of tropospheric delays, whereas a value greater than 2 indicates an apparent underestimation. A slope close to 1 in general suggests a good correction. The statistics show that tropospheric delays in 40% and 25% of the interferograms have been overestimated (i.e., Slope < 0) by the linear method and the CSS approach respectively, with those being underestimated (i.e., Slope ≥ 2) accounting for 36% and 51% respectively. However, our method improves the slopes of all interferograms, bringing them close to 1 after corrections (Figs. 3c and 3d), indicating that tropospheric noise is well resolved.

From the aspect of correlation, we can see that the improvement is also minor for both the linear and the CSS approaches, which are randomly distributed between -1 and 1 (Figs. 3e and 3f). Negative correlation values usually suggest an overestimation of tropospheric delays. The closer the correlation is to 1, the better the atmospheric correction. Similar to the analysis of fitting slope, the statistics on correlation also show that tropospheric delays in 40% and 25% of the interferograms have been overestimated (i.e., Correlation < 0) by the linear method and the CSS approach respectively. In contrast, our method can lead to a notable increase in correlation, as the corrected results align well with the simulated fault motions with high correlations of approximately 1 (Figs. 3e and 3e).

To summarize, our analysis of the RMS, fitting slope, and correlation prove that our method can well describe the spatiotemporal variabilities of tropospheric phase, as a consequence, providing high-quality interferograms almost free from tropospheric noise to support a reliable interpretation of tectonic motion.

C. Reduction in Mean Velocity and Displacement Time Series Fluctuations

In this section, we compare the mean velocities and displacement time series with and without the tropospheric corrections. To derive the average LOS deformation rate, we stack ~420 long temporal baseline (400 - 500 days) interferograms, with the results shown in Fig. 4. For the case without tropospheric correction, the average LOS rates exhibit similar spatial patterns to the true fault motion rates, but their magnitudes are almost twice as large (Fig. 4b1), especially to the south of the fault. This discrepancy might be related to temporal correlated topography-dependent atmospheric phases that cannot be eliminated during stacking. This explanation may also account for the relatively large deformation rate derived from the interferograms with the CSS corrections, as the temporal correlated topography-dependent atmospheric phases violate the assumption of the CSS (Fig. 4d1). In contrast, the mean velocities for the case with the empirical linear correction are closer to the true values, although their amplitudes are still slightly large (Fig. 4c1). This result suggests that the temporal correlated topography-dependent atmospheric phases are partially removed. In addition, the deformation rates results from the linear method show anomalous signals in the northwest region (Fig. 4c1). This may be attribute to spatially varying tropospheric noise that cannot be accounted for by the linear method. Fig. 4e1 demonstrates that our method estimates the atmospheric artifacts in interferograms well, as the mean LOS velocities from our method are consistent with the true rates in both amplitudes and spatial distributions.

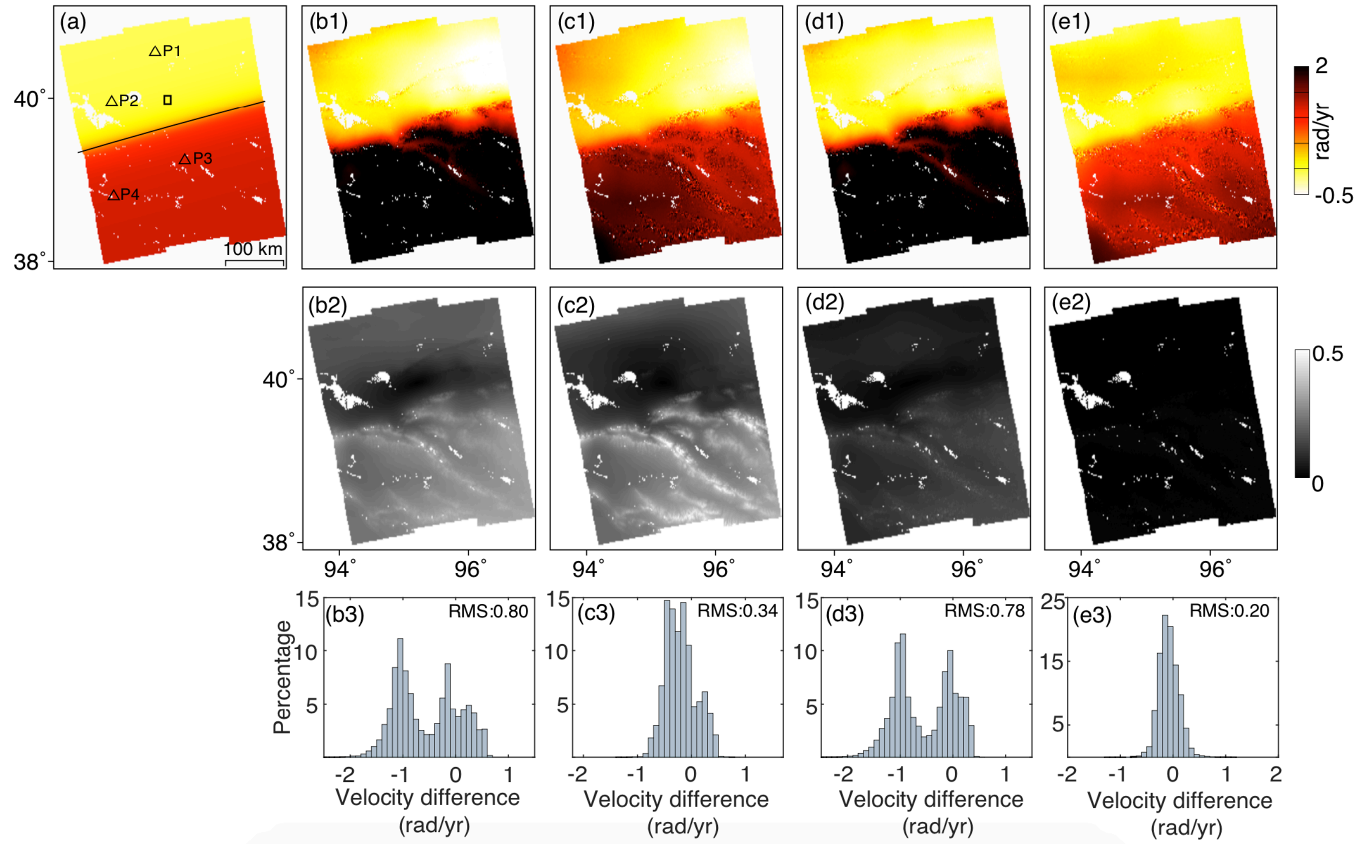

Fig. 4. Estimated mean LOS velocities. (a) Simulated mean LOS velocity due to fault motion. (b1) Mean LOS velocity inverted from interferograms without tropospheric correction, with the corresponding STD shown in (b2). (b3) Histogram of the velocity difference between (a) and (b1). (c1-c3)、(d1-d3) and (e1-e3) are same as (b1-b3) but corrected by the linear method, the CSS and our proposed method respectively.

The mean values of the STD of the LOS velocities derived from our method, the CSS, and the linear method are 0.001, 0.085, and 0.194 rad/yr respectively. These values are lower than the value of 0.209 rad/yr obtained without atmospheric corrections (Figs. 4b2, 4c2, 4d2 and 4e2). It should be noted that the phase measurements are referenced to a spatial reference window as specified, and that the STD of the LOS rate increase with the distance from the reference window, as the contribution of phase errors due to atmospheric and baseline errors increases. Even so, the RMS analysis at least suggests that our method outperforms the other involved methods.

We also calculate the RMS of the difference between the true rate map and the rate map recovered using different tropospheric correction methods (Figs. 4b3, 4c3, 4d3 and 4e3). The results show that our method effectively recovers fault motion signals, with a mean velocity difference that follows a normal distribution and an RMS value of 0.20 rad/yr. This value is significantly lower than the value of 0.80 rad/yr derived without tropospheric correction. The corresponding statistics for the linear and the CSS methods are 0.34 and 0.78 rad/yr respectively, which are larger than that of our method. These results clearly demonstrate that our method can robustly recover deformation even in the presence of strong atmospheric artifacts that are eight times the magnitude of the true deformation.

To further assess the impact of tropospheric delay on deformation retrieval and quantify the performance of our method, we also compare the derived displacement time series with the actual ones at four example pixels. We use the small baseline subset (SBAS) method [23] to conduct the time series analysis without temporal constraints on the displacement behavior. For the case without tropospheric correction, the derived displacements time series exhibit apparent fluctuations and largely deviate from the true values (Fig. 5). In contrast, our method significantly reduces displacement fluctuations, facilitating a more accurate extraction of ground deformation trends. Taking P3 as an example, the RMS of the difference between the retrieved and true displacement time series decreases from 7.58 rad before correction to 0.34 rad after correction, with a 95% reduction in RMS. As for the other two methods, there are still apparent fluctuations in the recovered displacement time series, particularly for P3 and P4, located south of the Altyn Tagh fault. As analyzed before, this might be due to the fact that the temporal correlated topography-dependent tropospheric noises are not adequately removed. Interestingly, we observe distinct variations in the amplitudes of the uncorrected displacement time series at P1-P4, located in different regions of the study area. This suggests spatial heterogeneity of the tropospheric noises, which poses a great challenge to the application of the empirical linear method. In contrast, our method demonstrates good consistency between the retrieved and true time series, indicating its effectiveness in estimating the spatial pattern and amplitude of the tropospheric artifact, enabling a more precise interpretation of tectonic activities.

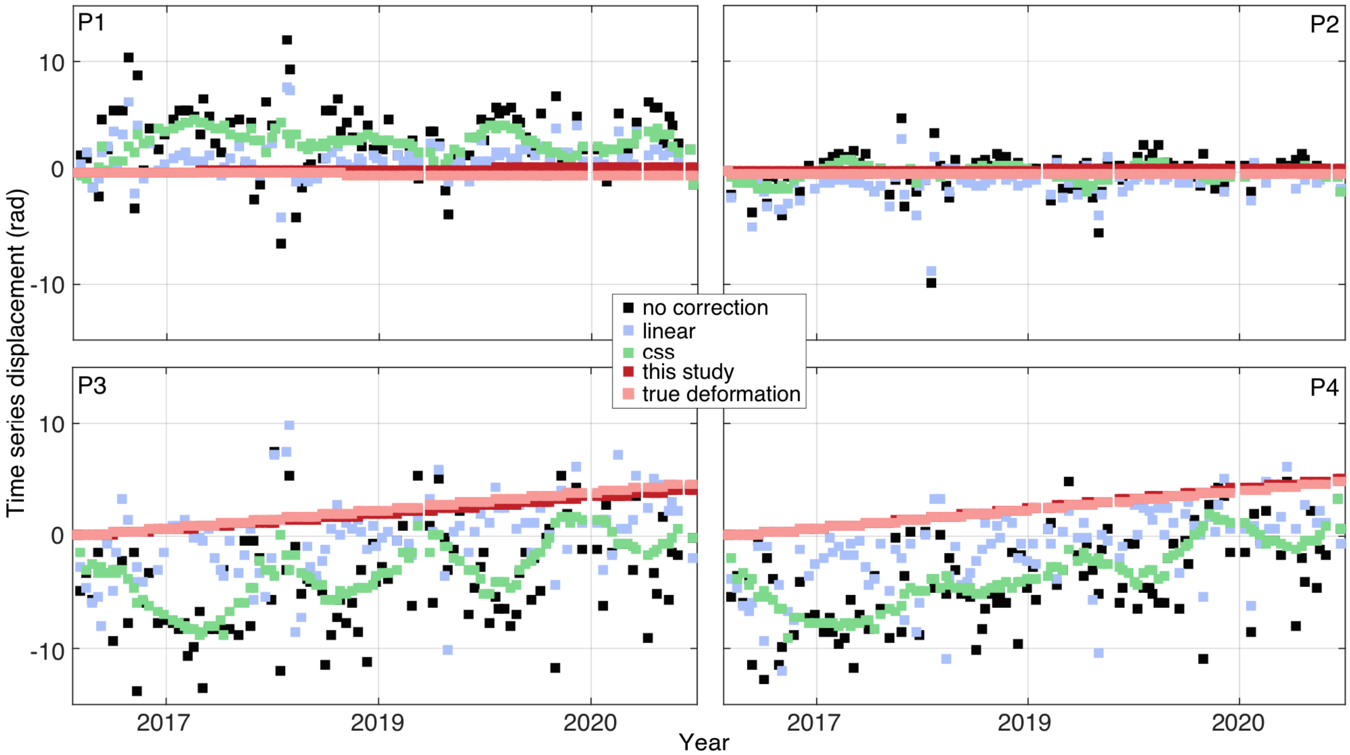

Fig. 5. Displacement time-series at the example pixels with their locations shown in Fig. 4a.

IV. Application to the Easternmost Altyn Tagh Fault Zone

In this section, we apply our method to the easternmost Altyn Tagh fault in the northern Tibetan Plateau (Fig. 6) to further examine its performance in practical application. As the fault is located at the border between the low Tarim Basin and the high Tibetan Plateau (with a ~6,000 m topographic relief), tropospheric artifacts here can be strong enough to overwhelm the real interseismic deformation signals (see two example interferograms in Fig. 6). In addition, interseismic deformation here is expected to correlate with the regional topography in space. Therefore, this region provides an ideal place to test the effectiveness of the tropospheric correction method.

A. Data Processing

We collect radar images from the ascending track 172 of the Sentinel-1 satellite to map the kinematic responses of the Earth’s surface to the fault motion of the easternmost section of the Altyn Tagh fault. To ensure full spatial coverage of the study area, we concatenate single-look-complex (SLC) images from two frames (i.e., 1307 and 1312) on the track, and finally, create 112 concatenated SLC images spanning from 04 April 2017 to 26 March 2021. We generate short-period interferograms with perpendicular baseline ≤ 100 m and temporal spanning ≤ 96 days (Fig. S1), and generate long-period interferograms with perpendicular baseline ≤ 100 m and temporal baseline between 400 and 500 days (Fig. S2). We adopt the Gamma software to process the SAR images into interferograms [42] and remove the topographic phase using the 30-m resolution Shuttle Radar Topography Mission digital elevation model [43]. We multi-look the original interferograms with 20 looks in range and 4 looks in azimuth directions. To reduce phase noise, we filter the interferograms twice using an adaptive filtering method [44] with a relatively small pixel window size of 32 × 32. Finally, we unwrap the interferogram phases [45] and geocode into the WGS84 coordinate system.

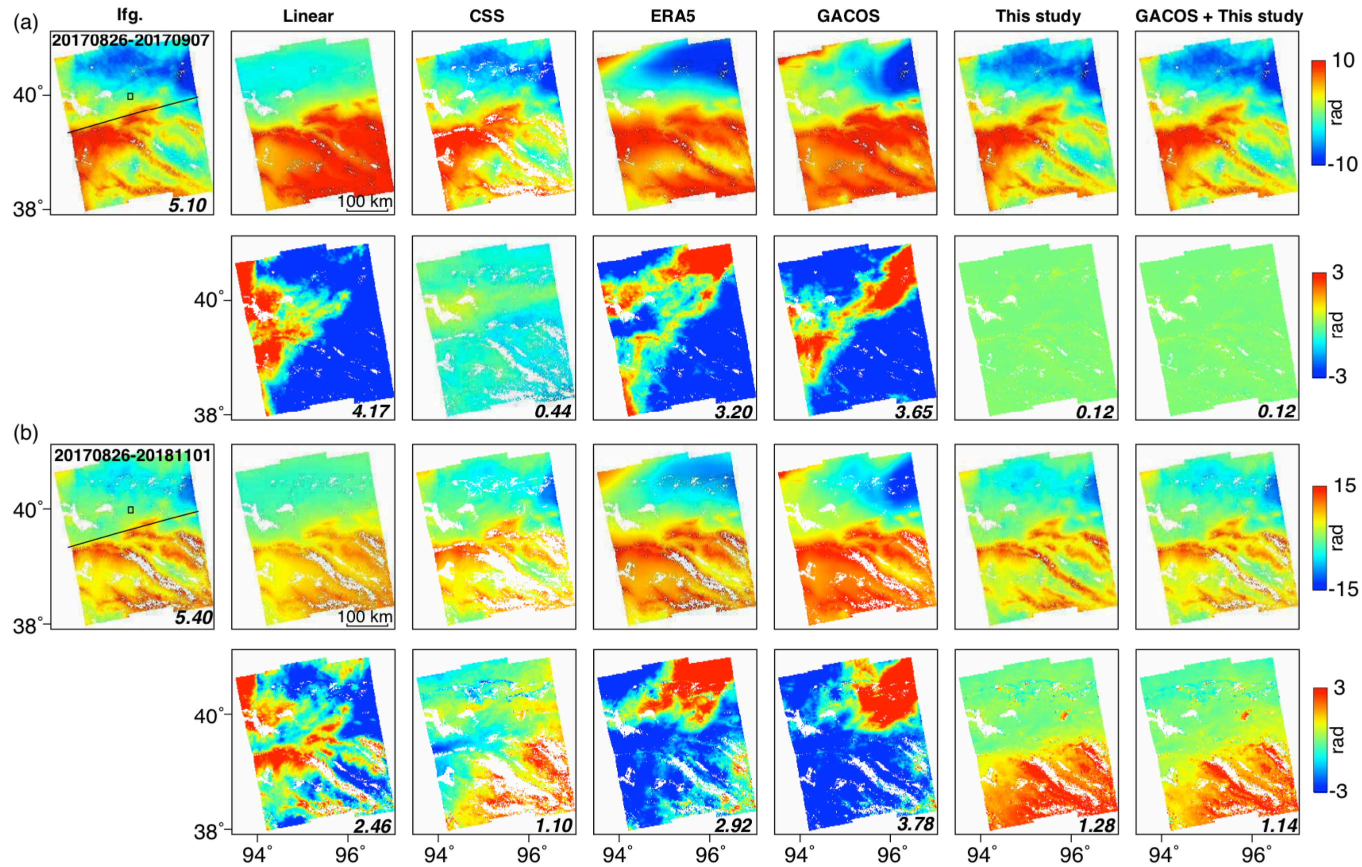

Fig. 6. Two example real interferograms to assess the quality of tropospheric corrections. (a) The first row shows an example interferogram with a short period of 12 days, along with the tropospheric delays estimated using different methods. The second row shows the corresponding interferograms after correction. (b) Same as (a), but for an example interferogram spanning a long period of 432 days. The standard deviations of the original interferogram and corresponding corrected ones are also labeled.

B. Tropospheric Phase Estimation

Based on the flow chart (Fig. 1), we first correct phase unwrapping errors in the real interferograms through a two-step procedure according to Section II-A. After that, we estimate tropospheric phases for each scene using unwrapping error-reduced interferograms with temporal baselines of ≤ 60 days (Fig. S1) and use these estimations to estimate and remove the tropospheric phases in all interferograms according to Section II-B. In addition to the linear and CSS corrections, to make a comprehensive comparison, we also correct interferograms using external data from ERA5 and GACOS [16-18] based on the TRAIN software [7], [29]. Two example interferograms with different temporal baselines are shown in Fig. 6, for convenience, we denote the example interferogram 20170826-20170907 as IFG 1 (short-period, 12 days), and interferogram 20170826-20181101 as IFG 2 (long-period, 432 days). For IFG 1, the STD is initially 5.10 rad, which decreases to 4.17, 0.44, 3.20, 3.65, and 0.12 rad after applying the linear, CSS, ERA5, GACOS, and our method respectively (Fig. 6a). As we can see from Fig. 6a, despite achieving STD reductions for all methods, apparent residuals (which are not expected for a short-period interferogram) are still present in the corrected results from the linear, CSS, ERA5, and GACOS methods, indicating these methods are less effective compared to our method. For the IFG 2, the STD decreases from an initial value of 5.40 rad to 2.46, 1.10, 2.92, 3.78, and 1.28 rad respectively after applying the corresponding corrections (Fig. 6b). While the CSS correction appears to perform better than our method using only the STD metric, visual inspection of the interferogram suggests that none of the other methods can accurately reflect the sense of left-lateral strike-slip motion of the Altyn Tagh fault. Therefore, evidence from the two example interferograms indicates that our method is the most accurate for predicting either the spatial pattern or the amplitude of the tropospheric phases among the investigated methods.

Except for the two example real interferograms, we look further at the relevant statistics for more interferograms. For the short-period (i.e., ≤ 60 days) interferograms with a total number of ~490, the scatter plots of the STD before and after the corrections (Fig. 7a) reveal that our method is the most effective, followed by the CSS approach, the GACOS model, the ERA5 model, and the empirical linear method. The statistics depicted in Fig. 7b reflect that after the corrections, 100%, 75%, 4%, 4%, and less than 1% of the interferograms have STD values of smaller than 1 rad using the above five correction methods, respectively. Furthermore, 100%, 94%, 29%, 22%, and 12% of the interferograms have achieved an STD reduction of great than 0.5 for the aforementioned five methods respectively, as illustrated in Figs. 7c and 7d.

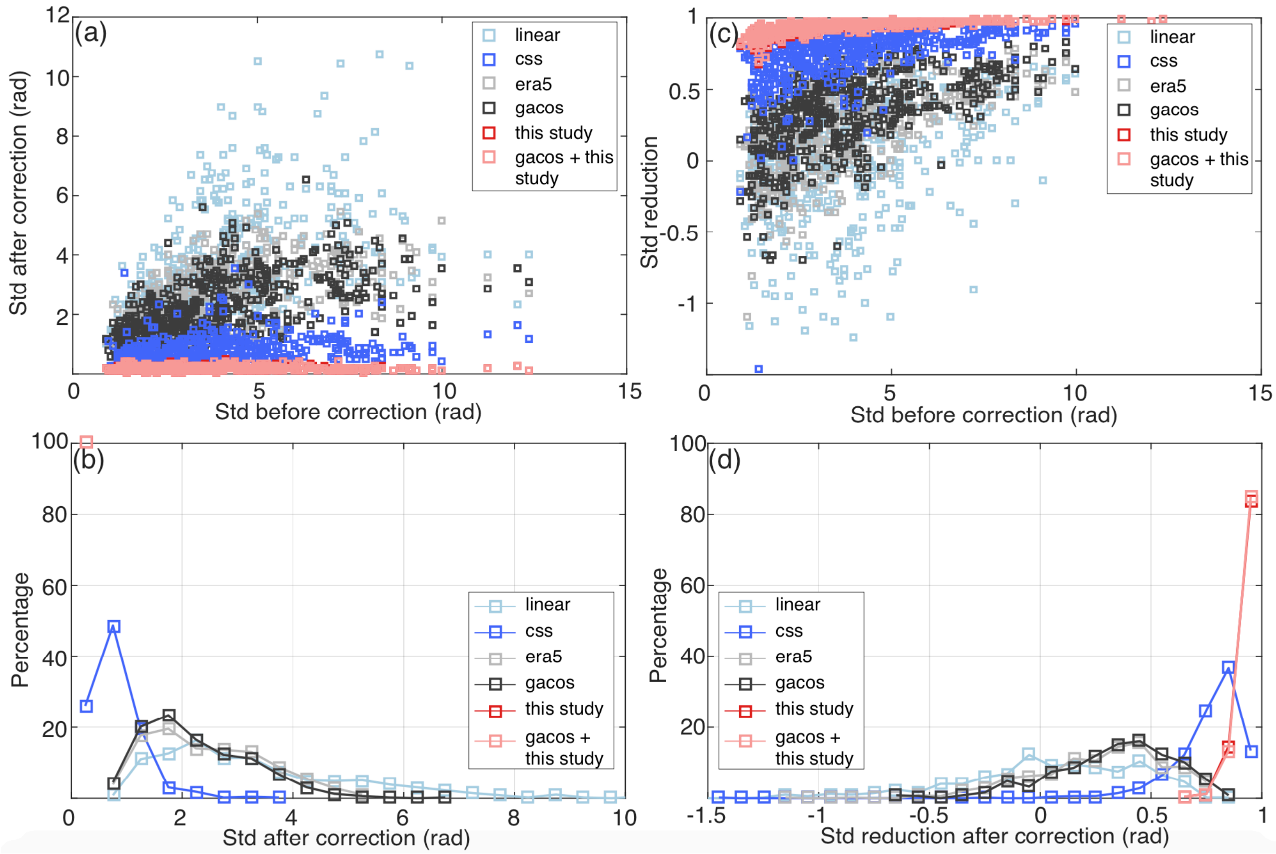

Fig. 7. Quality assessments of the atmospheric corrections on the short-period (i.e., ≤ 60 days) interferograms for the Altyn Tagh fault. (a) Scatter plots of standard deviations of the interferograms before and after the tropospheric corrections using different methods, with their statistical distributions shown in (b). (c) and (d) Same as (a) and (b) but for standard deviation reductions respectively.

For the long-period (i.e., 400 - 500 days) interferograms with a total number of ~420, the performances of the five correction methods are equivalent to those for the short-period interferograms (Fig. 8a), i.e., our method exhibits the best performance, followed by the CSS approach, the GACOS model, the ERA5 model, and the empirical linear method. According to the statistics presented in Fig. 8b, 100%, 61%, 29%, 20%, and 17% of the interferograms have a STD of no more than 2 rad after the corrections respectively. Moreover, the above methods have resulted in a STD reduction of great than 0.5 for 85%, 57%, 31%, 24%, and 15% of interferograms, as illustrated in Figs. 8c and 8d.

Interestingly, we find that the scatter plots of the STDs of the original interferograms and the STD reductions exhibit a logarithmic pattern (Figs. 7c and 8c). This means that the methods involved in this study, including our own, are particularly effective in correcting interferograms suffering from strong tropospheric delays. However, in cases where the tropospheric delays in the original interferograms vary smoothly in magnitude and space, corresponding to calm atmospheric conditions with relatively low initial STDs, the other four methods may occasionally yield an incorrect correction with negative STD reductions (Figs. 7 and 8). The improvement of InSAR deformation retrieval by our method could aid in the interpretation of strain accumulation and the assessment of earthquake hazard on faults.

This article has been accepted for publication in IEEE Transactions on Geoscience and Remote Sensing. This is the author's version which has not been fully edited and content may change prior to final publication. Citation information: DOI 10.1109/TGRS.2023.3296958

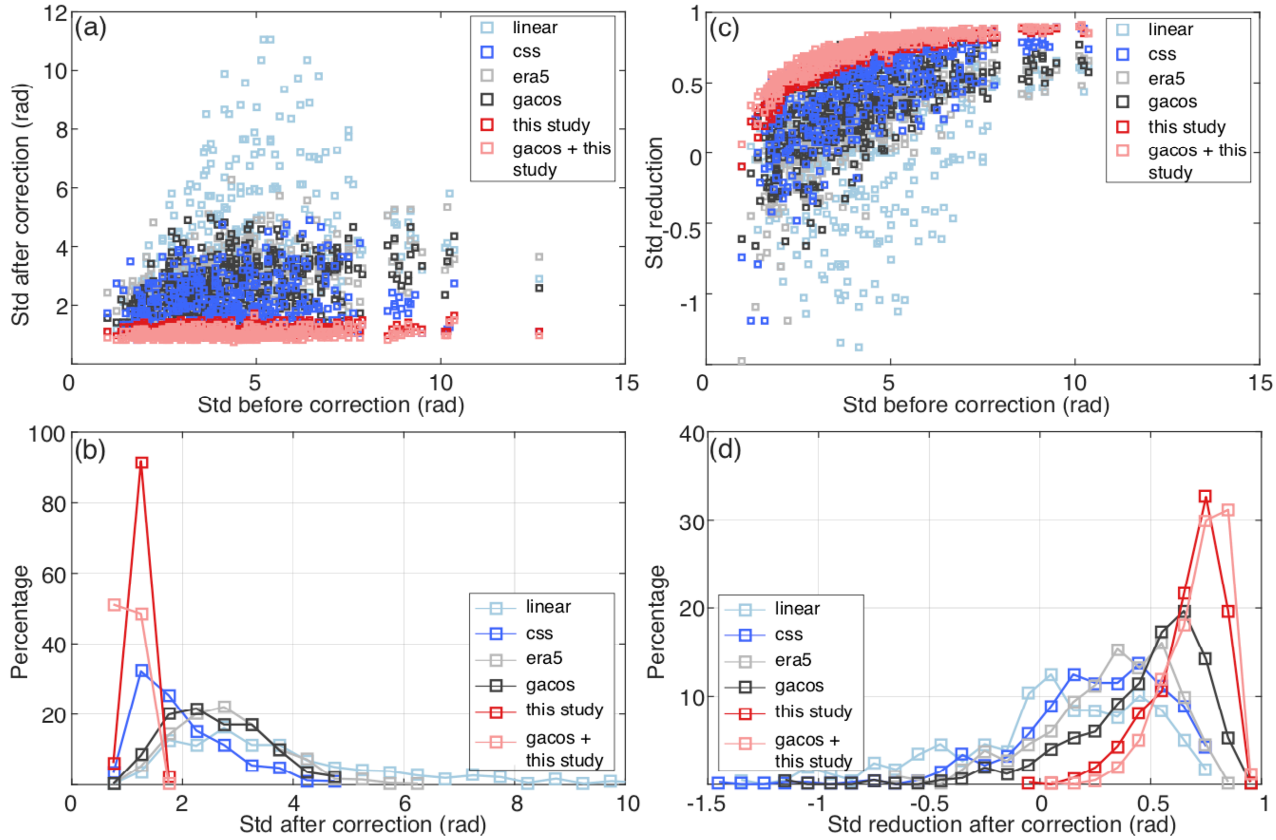

Fig. 8. Same as Fig. 7 but for the quality assessments of atmospheric corrections on the long-period (400 - 500 days) interferograms for the Altyn Tagh fault.

C. Displacement Time Series Analysis

In this section, we validate our method further by performing a comparison of the InSAR LOS time series with an independent data set, namely GNSS measurements [46]. To obtain the InSAR LOS displacement time series at the GNSS stations, we conduct time series analysis on the long temporal radar interferograms (400 - 500 days) using the SBAS method [23], but with no temporal constraint on the displacement behavior. We collect continuous GNSS displacements spanning the time period of InSAR observations from the GNSS data product service platform of China Earthquake Administration. We project the three-dimensional GNSS displacement time series onto the LOS based on the local azimuth and incidence angles of the SAR image. Because there are only two continuous stations (i.e., GSDH and GSAX) available in the region (Fig. 9), to ensure a solid comparison, we calculate the relative GNSS and InSAR LOS displacement time series between the two available continuous sites respectively. We can see that the InSAR LOS displacement time series without tropospheric corrections (light green dots in Fig. 9) show significant fluctuations in magnitude. As analyzed before, although the linear method, CSS approach, ERA5, and GACOS corrections reduce tropospheric delays to some extent, the resulting time series still display apparent fluctuations and fail to reflect the true relative time series between the two stations. The InSAR LOS displacement time series from our method (red dots in Fig. 9) exhibit good agreement with the GNSS LOS time series in temporal behavior. The consistent shift between the GNSS and InSAR LOS time series may be caused by systematic error in GNSS and/or residual tropospheric and orbital errors in InSAR [38], [47].

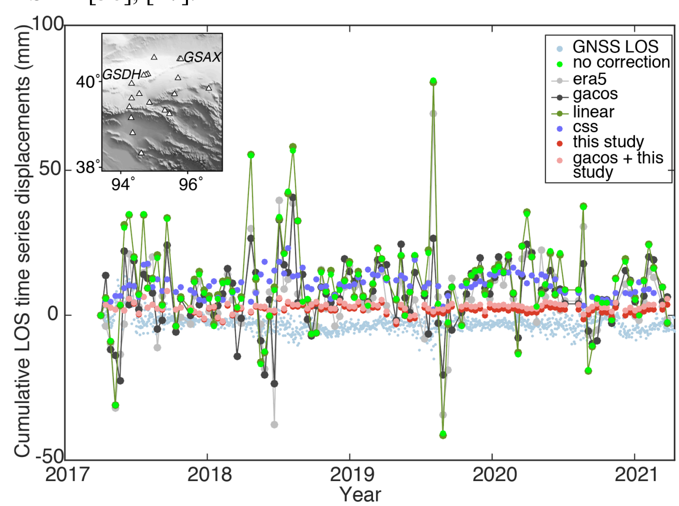

Fig. 9. Comparison of InSAR LOS time series with three-dimensional GNSS time series projected into the LOS. Note that the main panel shows the relative LOS time series between two continuous stations GSDH and GSAX. The inset map shows the locations of both continuous and campaign GNSS stations.

Aside from comparing relative displacement time series, we also compare the InSAR LOS rates and the GNSS LOS rates projected from the horizontal displacement fields of [46]. Note that these GNSS results are not from continuous stations but instead from regular GNSS monitoring surveyed once every 2 to 3 years. Additionally, for simplicity, we no longer analyze the InSAR LOS rates from the other methods as interferograms corrected by they still show significant variations. The InSAR LOS rates derived from our method reveal a clear strain gradient across the Altyn Tagh fault (Fig. 10c). The InSAR and GNSS LOS rates is generally consistent, with an RMS fitting residual of 1.42 mm/yr and a mean absolute difference (MAD) of 1.04 mm/yr (Fig. 10d). However, we note that the InSAR LOS rates on the south side of the fault exceed those of the GNSS LOS rates. This discrepancy is more evident in the results without tropospheric correction (Figs. 10a and 10b), with an RMS fitting residual of 2.23 mm/yr and an overall MAD of 2.01 mm/yr. We first exclude the reason that vertical deformation on the south of the Altyn Tagh fault was overlooked when projecting the GNSS displacements into the LOS. As previous studies, for example, [30] showed GNSS-measured vertical velocities in the region are mainly characterized by subsidence of no more than 2 mm/yr, while leveling data also demonstrated the subsidence is less than 0.3 mm/yr [48]. Therefore, the discrepancy between the InSAR LOS and GNSS LOS rates on the south side of the fault may not be due to vertical crustal motion, but rather the residual topography-correlated tropospheric artifact in interferograms, which are not corrected properly. For regions with strong stratified tropospheric noises, a preliminary tropospheric correction (such as GACOS) in combination with our method may be useful in improving the corrections of tropospheric delays, which will be further discussed in Section V-D.

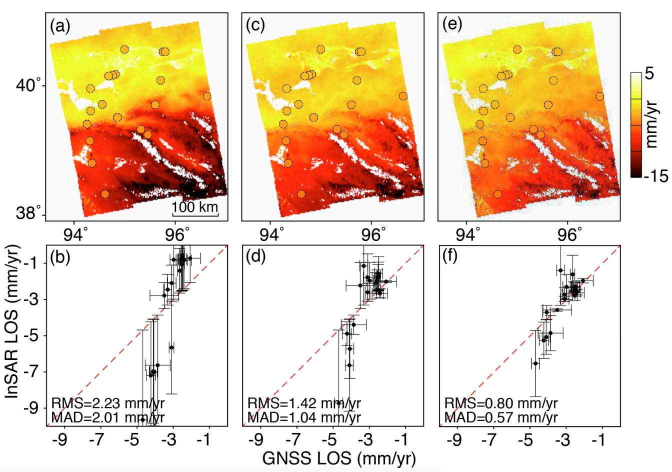

Fig. 10. Comparison of the estimated InSAR LOS mean velocities and the projected GNSS LOS velocities. (a) InSAR LOS mean velocity estimated from long-period (400 - 500 days) interferograms without the tropospheric correction, which has been tied to GNSS reference. Color-coded dots are the horizontal GNSS velocities projected onto the LOS direction. (b) Comparison between InSAR LOS and GNSS LOS displacements. Horizontal error bars represent the uncertainties of GNSS LOS velocities calculated from the uncertainties of GNSS horizontal velocities based on the law of error propagation, while we use the difference between InSAR LOS and GNSS LOS velocities to define the uncertainties of InSAR LOS velocities. The dashed red line is the one-to-one line for reference. (c-d and e-f) Same as (a-b) but for the mean velocities estimated from our method and a combination of the GACOS and our method respectively.

V. Discussion

A. Importance of Considering the Deformation Term for Our Method

Short-period interferograms are often used to map precipitable water vapors [37], and to derive tropospheric phases [21] due to their relatively higher percentage of pixels with high coherence. In these studies, the contribution of crustal deformation to phase is often assumed to be minor and ignored in modeling. However, at present, the impact of this practice on the estimation of relevant parameters remains unclear. Therefore, we conduct a test to examine whether the deformation term can be neglected when estimating the atmospheric phases using short temporal baseline interferograms.

Fig. 11a shows that if we do not consider the deformation term (denoted as Model 1), the estimated tropospheric phases depend on the threshold of Bt_short obviously. The amplitude of the corrected interferogram phase decreases as Bt_short increases, especially when Bt_short ≤ 60 days. Interferograms with longer temporal baselines are expected to have more phase contributions from interseismic deformation. Naturally, if we ignore the deformation term, these phases will be mistakenly treated as atmospheric noise, leading to an overestimation of the tropospheric noise. After considering the deformation term (denoted as Model 2), the tropospheric estimations become stable in both spatial distribution and amplitude when Bt_short ≥ 60 days, as shown in Fig. 11b.

We calculate the slope, correlation, and RMS of the difference between the recovered deformation and the true deformation with and without considering the deformation term. Their evolutions with Bt_short are then evaluated. The results are presented in Fig. 11c. In Model 1, it is evident that an increase in Bt_short results in a decrease in the slope, from 0.4 to ~0.18. This observation implies that without accounting for the deformation term, the fault motion is increasingly underestimated, while the atmospheric delays are increasingly overestimated. Conversely, for Model 2, the slope increases with Bt_short and eventually reaches a convergence of ~0.9 when Bt_short ≥ 60 days. The correlation for both Model 1 and Model 2 increases with Bt_short and approaches a convergence of 0.96 when Bt_short ≥ 36 days. The RMS of Model 1 increases until Bt_short = 60 days, where it converges to ~0.85 rad. In contrast, the RMS of Model 2 converges to a minimum value of 0.2 rad when Bt_short ≥ 36 days. If phase contributions from fault motion are not considered, they will be wrongly regarded as atmospheric noises. This can result in the partial removal of true deformation signals during the tropospheric corrections, especially if they also correlate with the regional topography. This erroneous removal is quite common in the retrieval of tectonic motion across contrasting elevation regions, such as in the Altyn Tagh fault zone. Therefore, we conclude that phase contributions from the interseismic deformation cannot be ignored even if short-period interferograms are used to estimate tropospheric delays.

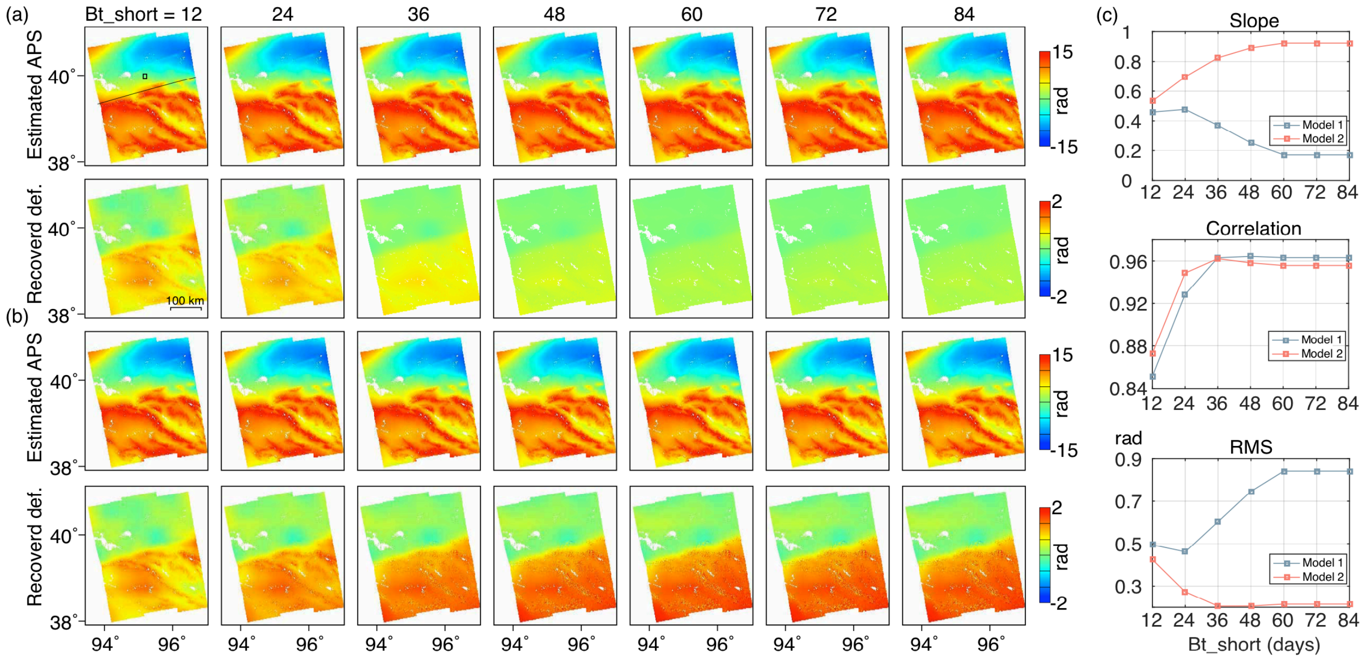

Fig. 11. An example simulated long-period interferogram (20170826-20181101) to evaluate the importance of considering the deformation rate during tropospheric estimations. (a) The first row shows the estimated tropospheric phase for the simulated interferogram in Fig. 2a1 with different thresholds of Bt_short, where the deformation term was not considered during this process (denoted as Model 1). The second row shows the corresponding corrected interferograms.(b) Same as (a) but with considering the deformation term when estimating the tropospheric phase (denoted as Model 2). (c) The fitting slope, correlation and RMS of the difference between the recovered deformation signal and the true one using Model 1 and Model 2.

B. Impacts of the Threshold of Bt_short on the Tropospheric Corrections

In this section, we examine the impacts of the selection of Bt_short on atmospheric corrections through the analysis of the slope, correlation, and RMS of the misfit difference between the recovered deformation signals and the simulated fault signals in long-period (400 - 500 days) interferograms. Fig. 12 shows that even though a larger Bt_short provides more observational data, its effect on atmospheric estimations is relatively insignificant as long as the deformation term (i.e., Model 2) is considered in the modeling. Our reasoning is asserted by the following observations. (i) No improvement is observed in the slopes and RMS for each interferogram when Bt_short $\geq$ 60 days, which converges to 1 and ~0.2 rad, respectively. The close to 1 slope and low RMS suggest that Model 2 provides a good description of the amplitude of the tropospheric noise (Figs. 12a and 12c). (ii) The correlation coefficient estimated for each interferogram converges to 0.92 when Bt_short $\geq$ 60 days. The close to 1 correlation suggests that Model 2 provides a good description of the spatial variabilities of the tropospheric noise (Fig. 12b). Therefore, a larger Bt_short value may not be necessary for estimating atmospheric delays from the perspectives of calculation accuracy and computational efficiency. We recommend using a threshold of Bt_short equal to five times the SAR image revisit time, which allows for generating interferograms between each epoch and five consecutive epochs in both forward and backward in time.

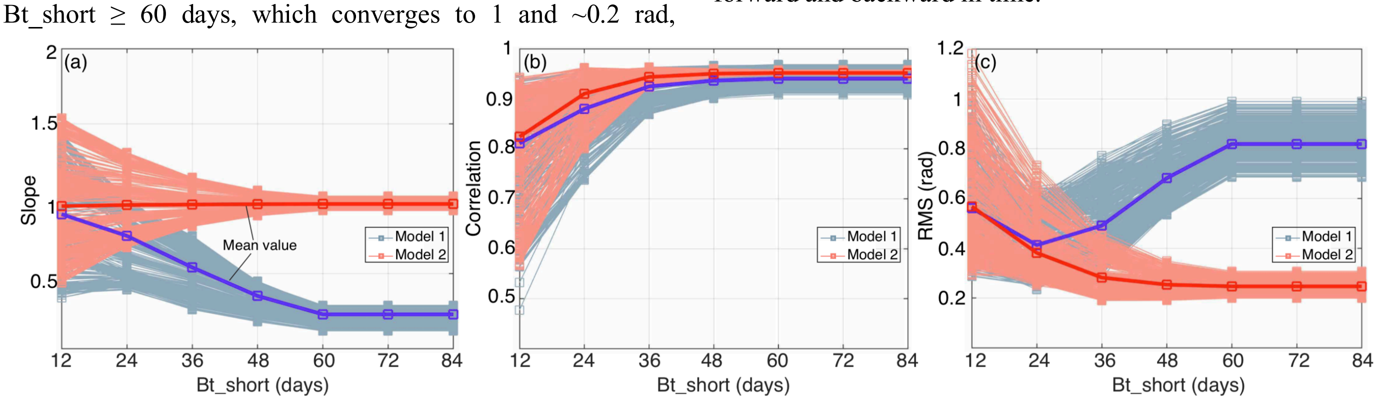

Fig. 12. Evaluation of the importance of considering the deformation rate and the effect of the selection of Bt_short on the performance of our tropospheric correction method. (a) Fitting slope, (b) correlation and (c) RMS of the difference between the synthetic fault motion signals and the recovered ones for long-period (400 - 500 days) interferograms based on Model 1 and Model 2. Each line represents one interferogram, the corresponding mean values for the three indicators are highlighted by the thick lines.

C. Significance of Fixing Unwrapping Errors for the Phase-based Tropospheric Corrections

Instead of simply discarding interferograms and/or pixels that contain unwrapping errors, here, we demonstrate the significance of correcting such errors phase-based tropospheric correction methods using an example real interferogram. In Fig. 13a, unwrapping errors are clearly observed in two main regions as outlined by dashed pink polygons in a short-period interferogram. Fig. 13d shows the unwrapping errors estimated for the interferogram using our proposed flow chart, and Fig. 13e displays the corrected outcome. After the correction of the unwrapping errors, we notice that the 2π phase jumps across the original interferogram vanish. Our strategy of combining the manual and automatic correction methods can accurately estimate the phase unwrapping errors in interferograms, even when they overlap in space between interferograms, which is a tricky case for either method alone.

To draw a comparison, we also adapt the conservative strategy to deal with unwrapping errors. To do this, we first compute the loop closure phases for all interferograms, followed by identifying the pixels that satisfy the criteria of $|\Delta\phi_{ij}^{obs} + \Delta\phi_{jm}^{obs} - \Delta\phi_{im}^{obs}| \geq 1$ rad for each loop closure phase (these pixels are defined as "error" pixels that have been incorrectly unwrapped) [49]. We mark these pixels in each loop closure with a flag value of 1, and finally combine the flag matrices from all loop closure phases to create a mask file for the pixels where the sum of the flag elements exceeds 10% of the total number of closure loops. Fig. 13b shows the generated mask file. Although the threshold for creating the mask file is already low, the interferogram that has been masked for unwrapping errors still contains numerous voids (Fig. 13c). Even so, we find that there are still some unwrapping errors that were not eliminated (as outlined by the dashed pink polygon in Fig. 13c).

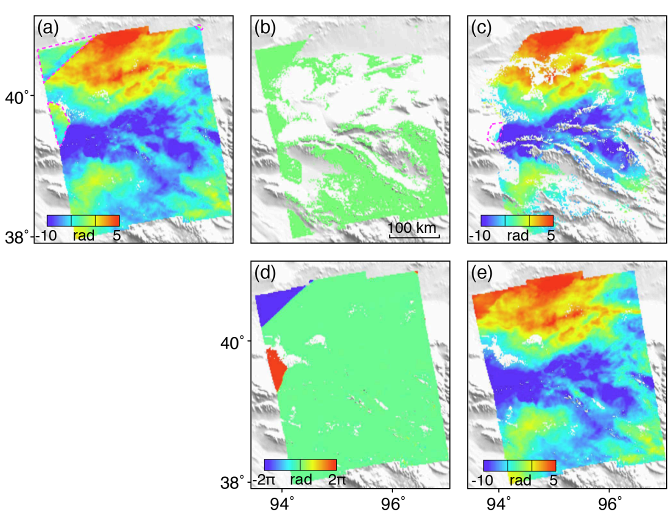

Fig. 13. Importance of correcting unwrapping errors in the interferogram. (a) An example real short-period interferogram (20180902-20180926) with apparent unwrapping errors as outlined by the dashed pink polygons. (b) Mask file created from loop closure phase information. (c) Masked result of (a) with (b). (d) Estimated unwrapping errors for (a) based on our flow chart. (e) Result of (a) with the estimated unwrapping errors removed.

In comparison to the conservative strategy, our proposed flow chart for addressing unwrapping errors has increased the number of effective pixels in an interferogram by 28% (Figs. 13c and 13e). The resulted interferograms with high-density effective pixels are expected to provide robust constraints on tropospheric estimations. While we acknowledge that our combined method may be time-consuming due to the inclusion of a manual procedure, it is a more generalizable and effective approach that can be used to produce high spatial resolution maps of interseismic deformation, which is crucial for investigating fault slip behavior and assessing seismic hazard.

D. Necessity of the Preliminary Tropospheric Error Correction for Our Method

In Section IV-C, we have clarified that the disparities between the GNSS LOS and InSAR LOS rates in the south of the Altyn Tagh fault are likely not due to vertical land motion. Instead, we speculate that the residual tropospheric noise could be the cause. For areas with strong stratified tropospheric noise, a combination of a preliminary tropospheric correction and our method may help improve the tropospheric corrections. To confirm this, we conduct another experiment where we use GACOS to correct the interferograms preliminarily, followed by our method to further mitigate residual tropospheric phases. We refer to this procedure as the combined method. While the individual short-period interferograms and displacement time series did not exhibit significant improvement compared to our method (Figs. 6 and 7), the combined method reduces the STD of the long-period interferograms (Figs. 6 and 8) and results in spatially smooth mean LOS rates (Fig. 10e). Additionally, the fitting residuals of the mean LOS rates improved significantly, particularly for stations located south of the fault (Fig. 10f). After the correction using the combined method, the overall RMS misfit difference decreases from 1.42 of our method to 0.80 mm/yr, and the MAD from 1.04 of our method to 0.57 mm/yr. Therefore, when interseismic deformation and tropospheric phases are both coupled with the regional topography in space, aiming for better mitigation of the complex tropospheric artifacts, we recommend conducting a preliminary correction, such as the one based on GACOS. The integration of two or more independent data/methods is expected to be more robust than using a single data/method [6].

E. Advantages and Limitations of Our Tropospheric Estimation Method

The tremendous development of InSAR missions in recent years has enabled us to study low-rate interseismic deformation using longer time series and over greater spatial scales. Particularly, the frequent and regular SAR measurements, provided by the current Sentinel-1satellites and upcoming satellites like NISAR, allow us to form a wealth of short-period interferograms. Based on these high-quality observations, our tropospheric correction method enables the community to estimate the tropospheric phases synchronously with SAR acquisitions in the temporal and spatial sampling. This can help highlight the low-rate interseismic signals hidden in the noisy interferograms. Different from the weather model-based and the other phase-based correction approaches, our method can better consider the variable statistical properties of the troposphere across an interferogram with a good description of the turbulent component. Our method can also prevent overestimation of the tropospheric phases when tectonic signals and tropospheric artifacts are both correlated with the topography. Our approach is therefore suitable for detecting interseismic displacements in cases where tropospheric phase dominates the interferograms.

We should acknowledge that our tropospheric estimation method is primarily oriented to the retrieval of interseismic deformation, as we assume a steady deformation rate for each pixel when solving for atmospheric delays. It may not be suitable for detecting non-steady deformation characterized by transient pulses such as those caused by fault creeping [49], [50], volcanic [51], and anthropological activities [52], [53]. In addition, we simply use equal weighting for all observations in the modeling, which may affect tropospheric estimates when there are significant variations between the observations [36], [54]. Note that phase components from the digital elevation model errors and other sources of noise may also affect the tropospheric estimations. Our method could be potentially enhanced if it further considers: (i) a time-varying strain model, and (ii) the different weight ratios among the observations. These need further studies in the future.

VI. Conclusions

In this study, we develop a novel phase-based InSAR tropospheric estimation method for the retrieval of interseismic deformation using high-quality short-period interferograms. Our method considers a steady linear deformation rate in the model to avoid overestimation of atmospheric phases when tectonic signals of interest are correlated with topography. We validate the performance of the proposed method using both synthetic and practical data and have the following findings:

1. The method can produce atmospheric phase estimates that are synchronized with SAR acquisitions in both temporal and spatial samplings, and thus enabling effective correction of tropospheric delays.
2. The phase contributions from the interseismic deformation cannot be ignored even if short-period interferograms are used to estimate tropospheric delays.
3. A threshold of Bt_short equal to five times the SAR image revisit time is recommended for our method when estimating the tropospheric delays.
4. Our preprocessing procedure for fixing unwrapping errors is important for the phase-based tropospheric correction method, leading to an apparent increase in the number of effective pixels in the interferogram.
5. In cases where tectonic deformation is strongly correlated with the topography, we recommend a combination of an initial tropospheric correction and our method to improve the corrections further.

One of the notable advantages of our method is that it does not require any external data, making it a potential real-time tropospheric correction tool, which is becoming increasingly important for automatic data processing for large-scale high-resolution tectonic velocity mapping.

Appendix A: Spatial and Temporal Baselines of Interferogram Networks

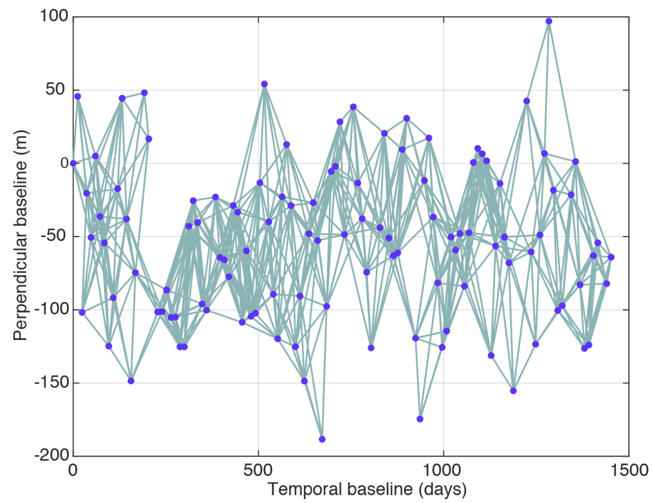

Fig. S1. Plots of spatial and temporal baselines for the short-period (12 – 96 days) interferograms from the descending track 172. Each blue dot represents one SAR acquisition and each line one interferogram.

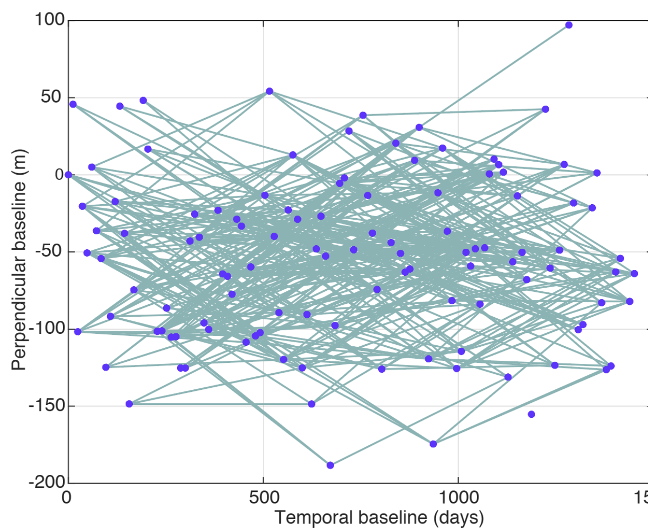

Fig. S2. Same as Fig. S1, but for the long-period (400 –500 days) interferograms.

Acknowledgment

We would like to thank two anonymous reviewers for their valuable comments. We thank Wei Xiong for providing us the continuous GNSS data and Kang Wang for providing us the code for common-scene-stacking. Horizontal GNSS displacements are available through [46]. We recognize the European Centre for medium range weather forecasts for providing the ERA5 products, which can be freely assessed from https://cds.climate.copernicus.eu. The Sentinel-1 data are

copyright of the European Space Agency (ESA) and are freely available through the Copernicus Open Access Hub (https://scihub.copernicus.eu). The GACOS product can be freely accessed from http://www.gacos.net. Figures are prepared using Generic Mapping Tools [55] and MATLAB. The code for the tropospheric correction method we developed in this study can be freely assessed from https://doi.org/10.5281/zenodo.7847743.

REFERENCES

[1] J. R. Elliott, R. J. Walters, and T. J. Wright, “The role of space-based observation in understanding and responding to active tectonics and earthquakes,” *Nat Commun*, vol. 7, no. 1, p. 13844, Dec. 2016.

[2] J. Biggs and T. J. Wright, “How satellite InSAR has grown from opportunistic science to routine monitoring over the last decade,” *Nat Commun*, vol. 11, no. 1, p. 3863, Aug. 2020.

[3] X. Ding, Z. Li, J. Zhu, G. Feng, and J. Long, “Atmospheric effects on InSAR measurements and their mitigation,” *Sensors*, vol. 8, no. 9, pp. 5426–5448, Sep. 2008.

[4] J. R. Elliott, J. Biggs, B. Parsons, and T. J. Wright, “InSAR slip rate determination on the Altyn Tagh fault, northern Tibet, in the presence of topographically correlated atmospheric delays,” *Geophys. Res. Lett.*, vol. 35, no. 12, p. n/a-n/a, Jun. 2008.

[5] K. Ebmeier, “Application of independent component analysis to multitemporal InSAR data with volcanic case studies,” *J. Geophys. Res. Solid Earth*, vol. 121, no. 12, pp. 8970–8986, Dec. 2016.

[6] Z.-F. Ma, S.-J. Wei, Y. Aoki, J.-H. Liu, and T. Huang, “A new spatiotemporal InSAR tropospheric noise filtering: An interseismic case study over central San Andreas fault,” *IEEE Trans. Geosci. Remote Sensing*, vol. 60, pp. 1–16, 2022.

[7] D. P. S. Bekaert, R. J. Walters, T. J. Wright, A. J. Hooper, and D. J. Parker, “Statistical comparison of InSAR tropospheric correction techniques,” *Remote Sens. Environ*, vol. 170, pp. 40–47, Dec. 2015.

[8] M.-P. Doin, C. Lasserre, G. Peltzer, O. Cavalié, and C. Doubre, “Corrections of stratified tropospheric delays in SAR interferometry: Validation with global atmospheric models,” *J. Appl. Geophys*, vol. 69, no. 1, pp. 35–50, Sep. 2009.

[9] K. D. Murray, D. P. S. Bekaert, and R. B. Lohman, “Tropospheric corrections for InSAR: Statistical assessments and applications to the central United States and Mexico,” *Remote Sens. Environ*, vol. 232, p. 111326, Oct. 2019.

[10] Z. Li, J. -P. Muller, P. Cross, E. J. Fielding, “Interferometric synthetic aperture radar (InSAR) atmospheric correction: GPS, Moderate Resolution Imaging Spectroradiometer (MODIS), and InSAR integration,” *J. Geophys. Res.*, vol. 110, no. B3, p. B03410, 2005.

[11] Z. Li, J. -P. Muller, P. Cross, P. Albert, J. Fischer, and R. Bennartz, “Assessment of the potential of MERIS near-infrared water vapour products to correct ASAR interferometric measurements,” *Int. J. Remote Sens.*, vol. 27, no. 2, pp. 349–365, Jan. 2006.

[12] Z. Li, E. J. Fielding, P. Cross, and J.-P. Muller, “Interferometric synthetic aperture radar atmospheric correction: GPS topography-dependent turbulence model,” *J. Geophys. Res.*, vol. 111, no. B2, p. n/a-n/a, Feb. 2006.

[13] Z. Li, E. J. Fielding, P. Cross, and R. Preusker, “Advanced InSAR atmospheric correction: MERIS/MODIS combination and stacked water vapour models,” *Int. J. Remote Sens.*, vol. 30, no. 13, pp. 3343–3363, Jul. 2009.

[14] Z. W. Li et al., “Correcting atmospheric effects on InSAR with MERIS water vapour data and elevation-dependent interpolation model: Correcting atmospheric effects on InSAR,” *Geophys. J. Int.*, vol. 189, no. 2, pp. 898–910, May 2012.

[15] R. Jolivet et al., “Improving InSAR geodesy using global atmospheric models,” *J. Geophys. Res. Solid Earth*, vol. 119, no. 3, pp. 2324–2341, Mar. 2014.

[16] C. Yu, Z. Li, and N. T. Penna, “Interferometric synthetic aperture radar atmospheric correction using a GPS-based iterative tropospheric decomposition model,” *Remote Sens. Environ*, vol. 204, pp. 109–121, Jan. 2018.

[17] C. Yu, Z. Li, N. T. Penna, and P. Crippa, “Generic atmospheric correction model for interferometric synthetic aperture radar observations,” *J. Geophys. Res. Solid Earth*, vol. 123, no. 10, pp. 9202–9222, Oct. 2018.

[18] C. Yu, N. T. Penna, and Z. Li, “Generation of real-time mode high-resolution water vapor fields from GPS observations,” *J. Geophys. Res. Atmos.*, vol. 122, no. 3, pp. 2008–2025, Feb. 2017.

[19] S. T. H. Yip, J. Biggs, and F. Albino, “Reevaluating volcanic deformation using atmospheric corrections: Implications for the magmatic system of Agung volcano, Indonesia,” *Geophys. Res. Lett.*, vol. 46, no. 23, pp. 13704–13711, Dec. 2019.

[20] A. L. Parker et al., “Systematic assessment of atmospheric uncertainties for InSAR data at volcanic arcs using large-scale atmospheric models: Application to the Cascade volcanoes, United States,” *Remote Sens. Environ*, vol. 170, pp. 102–114, Dec. 2015.

[21] L. Shen, A. Hooper, and J. Elliott, “A spatially varying scaling method for InSAR tropospheric corrections using a high-resolution weather model,” *J. Geophys. Res. Solid Earth*, vol. 124, no. 4, pp. 4051–4068, Apr. 2019.

[22] A. Ferretti, C. Prati, and F. Rocca, “Permanent scatterers in SAR interferometry,” *IEEE Trans. Geosci. Remote Sensing*, vol. 39, no. 1, pp. 8–20, Jan. 2001.

[23] P. Berardino, G. Fornaro, R. Lanari, and E. Sansosti, “A new algorithm for surface deformation monitoring based on small baseline differential SAR interferograms,” *IEEE Trans. Geosci. Remote Sensing*, vol. 40, no. 11, pp. 2375–2383, Nov. 2002.

[24] A. Hooper, P. Segall, and H. Zebker, “Persistent scatterer interferometric synthetic aperture radar for crustal deformation analysis, with application to Volcán Alcedo, Galápagos,” *J. Geophys. Res.*, vol. 112, no. B7, p. B07407, Jul. 2007.

[25] H. Liang, L. Zhang, X. Ding, Z. Lu, and X. Li, “Toward mitigating stratified tropospheric delays in multitemporal InSAR: A quadtree aided joint model,” *IEEE Trans. Geosci. Remote Sensing*, vol. 57, no. 1, pp. 291–303, Jan. 2019.

[26] T. J. Wright, B. Parsons, P. C. England, and E. J. Fielding, “InSAR observations of low slip rates on the major faults of western Tibet,” *Science*, vol. 305, no. 5681, pp. 236–239, Jul. 2004.

[27] Y. N. Lin, M. Simons, E. A. Hetland, P. Muse, and C. DiCaprio, “A multiscale approach to estimating topographically correlated propagation delays in radar interferograms,” *Geochem. Geophys. Geosyst.*, vol. 11, no. 9, p. Q09002, Sep. 2010.

[28] Y. Kang, Z. Lu, C. Zhao, Y. Xu, J. Kim, and A. J. Gallegos, “InSAR monitoring of creeping landslides in mountainous regions: A case study in Eldorado national forest, California,” *Remote Sens. Environ*, vol. 258, p. 112400, Jun. 2021.

[29] D. P. S. Bekaert, A. Hooper, and T. J. Wright, “A spatially variable power law tropospheric correction technique for InSAR data,” *J. Geophys. Res. Solid Earth*, vol. 120, no. 2, pp. 1345–1356, Feb. 2015.

[30] H. Liang, L. Zhang, Z. Lu, and X. Li, “Correction of spatially varying stratified atmospheric delays in multitemporal InSAR,” *Remote Sens. Environ*, vol. 285, p. 113382, Feb. 2023.

[31] J. Biggs, T. Wright, Z. Lu, and B. Parsons, “Multi-interferogram method for measuring interseismic deformation: Denali fault, Alaska,” *Geophys. J. Int.*, vol. 170, no. 3, pp. 1165–1179, Sep. 2007.

[32] Y. Morishita, M. Lazecky, T. Wright, J. Weiss, J. Elliott, and A. Hooper, “LiCSBAS: An open-source InSAR time series analysis package integrated with the LiCSAR automated Sentinel-1 InSAR processor,” *Remote Sens.*, vol. 12, no. 3, p. 424, Jan. 2020.

[33] Wegmüller, C. Magnard, C. Werner, T. Strozzi, R. Caduff, and A. Manconi, “Methods to avoid being affected by non-zero closure phase in InSAR time series analysis in a multi-reference stack,” *Procedia Computer Science*, vol. 181, pp. 511–518, 2021.

[34] Q. Ou et al., “Large-scale interseismic strain mapping of the NE Tibetan Plateau from Sentinel-1 interferometry,” *J. Geophys. Res. Solid Earth*, vol. 127, no. 6, Jun. 2022.

[35] X. Xu and D. T. Sandwell,“Towards absolute phase recovery with InSAR: correcting for earth tides and phase unwrapping ambiguities,’’ *IEEE Trans. Geosci. Remote Sens.*, vol. 58, no. 1, pp. 726-733, Jan. 2020.

[36] Z. Yunjun, H. Fattahi, and F. Amelung, “Small baseline InSAR time series analysis: Unwrapping error correction and noise reduction,” *Computers & Geosciences*, vol. 133, p. 104331, Dec. 2019.

[37] Y. Cao, S. Jónsson, and Z. Li, “Advanced InSAR tropospheric corrections from global atmospheric models that incorporate spatial stochastic properties of the troposphere,” *J. Geophys. Res. Solid Earth*, vol. 126, no. 5, May 2021.

[38] Xu, D. T. Sandwell, E. Klein, and Y. Bock, "Integrated Sentinel-1 InSAR and GNSS time-series along the san Andreas fault system," *J. Geophys. Res. Solid Earth*, vol. 126, no. 11, Nov. 2021.

[39] J. C. Savage and R. O. Burford, "Geodetic determination of relative plate motion in central California," *J. Geophys. Res.*, vol. 78, no. 5, pp. 832–845, Feb. 1973.

[40] E. Tymofyeyeva and Y. Fialko, "Mitigation of atmospheric phase delays in InSAR data, with application to the eastern California shear zone: ATMOSPHERIC PHASE DELAYS," *J. Geophys. Res. Solid Earth*, vol. 120, no. 8, pp. 5952–5963, Aug. 2015.

[41] K. Wang and Y. Fialko, "Observations and modeling of coseismic and postseismic deformation due to the 2015 Mw 7.8 Gorkha (Nepal) earthquake," *J. Geophys. Res. Solid Earth*, vol. 123, no. 1, pp. 761–779, Jan. 2018.

[42] C. Werner, U. Wegmüller, T. Strozzi, and A. Wiesmann, "GAMMA SAR and interferometric processing software," *Proceeding of ERS ENVISAT Symposium*. 16–20 Oct. 2000.

[43] G. Farr et al., "The shuttle radar topography mission," *Rev. Geophys.*, vol. 45, no. 2, p. *Rev. Geophys*., May 2007.

[44] R. M. Goldstein and C. L. Werner, "Radar interferogram filtering for geophysical applications," *Geophys. Res. Lett.*, vol. 25, no. 21, pp. 4035–4038, Nov. 1998.

[45] C. W. Chen and H. A. Zebker, "Network approaches to two-dimensional phase unwrapping: intractability and two new algorithms," *J. Opt. Soc. Am. A*, vol. 17, no. 3, p. 401, Mar. 2000.

[46] M. Wang and Z. Shen, "Present-day crustal deformation of continental China derived from GPS and its tectonic implications," *J. Geophys. Res. Solid Earth*, vol. 125, no. 2, Feb. 2020.

[47] Y. Li, J. Nocquet, X. Shan, and X. Song, "Geodetic observations of shallow creep on the Laohushan-Haiyuan fault, northeastern Tibet," *J. Geophys. Res. Solid Earth*, vol. 126, no. 6, Jun. 2021.

[48] Y. Wu et al., "High-precision vertical movement and three-dimensional deformation pattern of the Tibetan Plateau," *J. Geophys. Res. Solid Earth*, vol. 127, no. 4, Apr. 2022.

[49] E. Hussain, A. Hooper, T. J. Wright, R. J. Walters, and D. P. S. Bekaert, "Interseismic strain accumulation across the central North Anatolian fault from iteratively unwrapped InSAR measurements," *J. Geophys. Res. Solid Earth*, vol. 121, no. 12, pp. 9000–9019, Dec. 2016.

[50] R. Jolivet, M. Simons, P. S. Agram, Z. Duputel, and Z.-K. Shen, "Aseismic slip and seismogenic coupling along the central San Andreas fault," *Geophys. Res. Lett.*, vol. 42, no. 2, pp. 297–306, Jan. 2015.

[51] Z. Lu, T. Masterlark, and D. Dzurisin, "Interferometric synthetic aperture radar study of Okmok volcano, Alaska, 1992-2003: Magma supply dynamics and postemplacement lava flow deformation," *J. Geophys. Res.*, vol. 110, no. B2, Feb. 2005.

[52] S. Wang et al., "Three Mw ≥ 4.7 Earthquakes within the Changning (China) shale gas field ruptured shallow faults intersecting with hydraulic fracturing wells," *J. Geophys. Res. Solid Earth*, vol. 127, no. 2, Feb. 2022.

[53] S. Wang, G. Jiang, M. Weingarten, and Y. Niu, "InSAR evidence indicates a link between fluid injection for salt mining and the 2019 Changning (China) earthquake sequence," *Geophys. Res. Lett.*, vol. 47, no. 16, Aug. 2020.

[54] R. Emardson, M. Simons, and F. H. Webb, "Neutral atmospheric delay in interferometric synthetic aperture radar applications: Statistical description and mitigation," *J. Geophys. Res.*, vol. 108, no. B5, May 2003.

[55] P. Wessel, W. H. F. Smith, R. Scharroo, J. Luis, and F. Wobbe, "Generic mapping tools: Improved version released," *Eos Trans. AGU*, vol. 94, no. 45, pp. 409–410, Nov. 2013.

Shuai Wang received the M.S. degree in geodesy and surveying engineering from the College of Geological Engineering and Geomatics, Chang'an University, Xi'an, China, in 2015, and the Ph.D. degree in geodesy and surveying engineering from the School of Geodesy and Geomatics, Wuhan University, Wuhan, China, in 2019.

From 2017 to 2018, he worked as a Research Assistant at the Department of Land Surveying and Geo-informatics in The Hong Kong Polytechnic University, Hong Kong, China. Currently he holds the position of a Lecture at the School of Geomatics Science and Technology, Nanjing Tech University, Nanjing, China. His currently research interests focus on earthquake-cycle deformation and induced deformation caused by industrial activities, utilizing interferometric synthetic aperture radar and Global Navigation Satellite System.

Zhong Lu (Senior Member, IEEE) received the B.S. and M.S. degrees from Peking University, Beijing, China, in 1989 and 1992, respectively, and the Ph.D. degree from the University of Alaska Fairbanks, Fairbanks, AK, USA, in 1996.

He is currently a Professor and the Endowed Shuler-Foscue Chair with the Huffington Department of Earth Sciences, Southern Methodist University, Dallas, TX, USA. He is also a Principal Investigator of projects funded by NASA, ESA, JAXA, DLR, and USGS on the study of land surface deformation using satellite interferometric synthetic aperture radar (InSAR) imagery. He has authored more than 45 and coauthored 90 peer-reviewed journal articles and book chapters focused on InSAR techniques and applications. His research interests include technique developments of SAR, InSAR, and their applications on natural hazard monitoring and natural resource characterization.

Bin Wang received the M.S. degree in geodesy and surveying engineering from the China University of Mining and Technology, Xuzhou, China, in 2013, and the Ph.D. degree in geodesy and surveying engineering from the School of Geodesy and Geomatics, Wuhan University, Wuhan, China, in 2017.

From 2015 to 2016, he was an Exchange Visitor supported by DAAD Thematic Network Project with the Institute of Geodesy, University of Stuttgart, Stuttgart, Germany. He is currently an Associate Professor with the School of Geomatics Science and Technology, Nanjing Tech University, Nanjing, China. His research interests include generalized total least-squares algorithms, point cloud data and InSAR data processing.

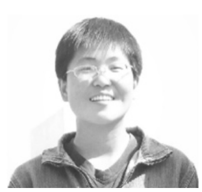

Yufen Niu received the M.S. and Ph.D. degrees from the College of Geological Engineering and Geomatics, Chang'an University, Xi'an in 2015 and 2020, respectively. From November, 2017 to November, 2019, she was a Visiting Ph.D. Student with the Southern Methodist University (SMU), Dallas, USA.

She is currently working as a Lecture at the Hebei University of Engineering since 2020. Her research focuses on mapping volcano deformation, examining magma supply dynamics, and monitoring landslide using InSAR imagery and numerical modeling.

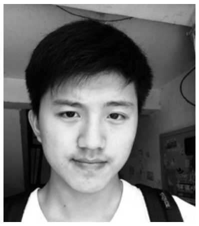

Chuang Song received the B.S. degree in Geomatics from Southwest Jiaotong University, Chengdu, China, in 2015, the M.Sc. degree in Geodesy from Wuhan University, Wuhan, China, in 2018, and the Ph.D degree from Newcastle University, Newcastle upon Tyne, UK, in 2022.

He is currently a Lecturer with the College of Geological Engineering and Geomatics, Chang'an University, Xi'an, China. His research interest includes the processing of satellite radar data and its application in the study of natural hazards (such as landslides and earthquakes).

Xing Li received the B.S. degree in geology from the China University of Petroleum, Beijing, China, in 2012, and the M.Sc. degree in surveying from The Hong Kong Polytechnic University, Hong Kong, in 2018. She is currently pursuing the Ph.D. degree with the King Abdullah University of Science and Technology, Thuwal, Saudi Arabia.

Her research interests include using interferometric synthetic aperture radar to monitor crustal deformation.

Zhang-Feng Ma received the B.S. degree in Geomatics Engineering from Nanjing University of Technology, Nanjing, China, in 2017, the M.Sc. degree in Geomatics Engineering from Hohai University, Nanjing, China, in 2019 and the Ph.D. degree in Geodesy from Hohai University, Nanjing, China, in 2022.

Currently he is a Research Fellow in Earth Observatory of Singapore, Nanyang Technological University, Singapore. His research interests include interferometric synthetic aperture radar and its application for monitoring and modelling interseismic displacements.

Caijun Xu received the M.S. and Ph.D. degrees from the Wuhan Technical University of Surveying and Mapping Geodesy, in 1988 and 1994, respectively.

He is currently a specially-appointed Professor in the Cheung Kong Scholars Program at the School of Geodesy and Geomatics, Wuhan University, Wuhan, China. He serves as the deputy director of the Key Laboratory of Geospatial Environment and Geodesy under the Ministry of Education, China, and the deputy director of the Key Laboratory of Geophysical Geodesy and Natural Resources under the Ministry of Natural Resources, China. His ongoing research focuses on studying the tectonic deformation in the Tibetan Plateau and its surroundings and investigating human-induced seismic and crustal deformation in the Sichuan Basin through multi-source observations from space geodesy and seismic data.